Chapter 5
Antennas and Arrays

This chapter opens with a brief review of some basic considerations of antennas. The main part of the chapter is concerned with the configurations of antennas in interferometers and synthesis arrays. It is convenient to classify array designs as follows:

1. Arrays with nontracking antennas
2. Interferometers and arrays with antennas that track the sidereal motion of a source:

   - Linear arrays
   - Arrays with open-ended arms (crosses, T-shaped arrays, and Y-shaped arrays)
   - Arrays with closed configurations (circles, ellipses, and Reuleaux triangles)
   - VLBI arrays
   - Planar arrays.

Examples of these types of arrays are described, and their spatial transfer functions (i.e., spatial sensitivities) are compared. Other concerns include the size and number of antennas needed in an array. Also discussed is the technique of forming images from direct Fourier transformation of the electric field on an aperture.

5.1 Antennas

The subject of antennas is well covered in numerous books; see Further Reading at the end of this chapter. Baars (2007) gives an informative review of parabolic antennas, including details of testing and surface adjustment. Here, we are concerned with the special requirements of antennas for radio astronomy. As discussed in Chap. 1, early radio astronomy antennas operated mainly at meter wavelengths and often consisted of arrays of dipoles or parabolic-cylinder reflectors. These had large areas,

but the operating wavelengths were long enough that beamwidths were usually of order 1° or more. For detection and cataloging of sources, satisfactory observations could be obtained during the passage of a source through a stationary beam or interferometer fringe pattern. Thus, it was not always necessary for such antennas to track the sidereal motion of a source. More recent meter-wavelength systems use dipole arrays with computer-controlled phasing to provide tracking beams [see, e.g., Koles et al. (1994) and Lonsdale et al. (2009)]. For higher frequencies, synthesis arrays use tracking antennas that incorporate equatorial or altazimuth mounts.

The requirement for high sensitivity and angular resolution has resulted in the development of large arrays of antennas. Such instruments are usually designed to cover a range of frequencies. For centimeter-wavelength instruments, the coverage typically includes bands extending from a few hundred megahertz to some tens of gigahertz. For such frequency ranges, the antennas are most often parabolic or similar-type reflectors, with separate feeds for the different frequency bands. In addition to wide frequency coverage, another advantage of the parabolic reflector is that all of the power collected is brought, essentially without loss, to a single focus, which allows full advantage to be taken of low-loss feeds and cryogenically cooled input stages to provide the maximum sensitivity.

Figure 5.1 shows several focal arrangements for parabolic antennas, of which the Cassegrain is perhaps the most often used. The Cassegrain focus offers a number of advantages. A convex hyperbolic reflector intercepts the radiation just before it reaches the prime focus and directs it to the Cassegrain focus near the vertex of the main reflector. Sidelobes resulting from spillover of the beam of the feed around the edges of the subreflector point toward the sky, for which the noise temperature is generally low. With a prime-focus feed, the sidelobes resulting from spillover around the main reflector point toward the ground and thus result in a higher level of unwanted noise pickup. The Cassegrain focus also has the advantage that in all but the smallest antennas, an enclosure can be provided behind the main reflector to
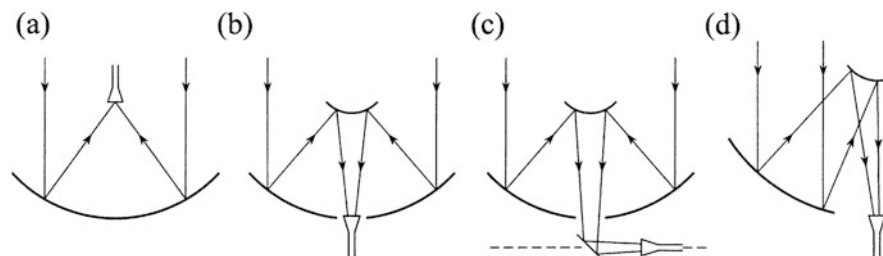

Fig. 5.1 Focus arrangements of reflector antennas: (**a**) prime focus; (**b**) Cassegrain focus; (**c**) Naysmith focus; (**d**) offset Cassegrain. With the Naysmith focus, the feed horn is mounted on the alidade structure below the elevation axis (indicated by the dashed line), and for a linearly polarized signal, the angle of polarization relative to the feed varies with the elevation angle. In some other arrangements, for example, beam-waveguide antennas (not shown), there are several reflectors, including one on the azimuth axis, which allows the feed horn to remain fixed relative to the ground. The polarization then rotates relative to the feed for both azimuth and elevation motions.

accommodate the low-noise input stages of the electronics. However, the aperture of the feed for a prime-focus location is less than that for a feed at the Cassegrain focus, and as a result, the feeds for the longer wavelengths are often at the prime focus.

The Cassegrain design also allows the possibility of improving the aperture efficiency by shaping the two reflectors of the antenna (Williams 1965). The principle involved can best be envisioned by considering the antenna in transmission. With a conventional hyperboloid subreflector and parabolic main reflector, the radiation from the feed is concentrated toward the center of the antenna aperture, whereas for maximum efficiency, the electric field should be uniformly distributed. If the profile of the subreflector is slightly adjusted, more power can be directed toward the outer part of the main reflector, thus improving the uniformity. The main reflector must then be shaped to depart slightly from the parabolic profile to regain uniform phase across the wavefront after it leaves the main reflector. This type of shaping is used, for example, in the antennas of the VLA in New Mexico, for which the main reflector is 25 m in diameter. For the VLA, the rms difference between the reflector surfaces and the best fit paraboloid is ~ 1 cm, so the antennas can be used with prime-focus feeds for wavelengths longer than ~ 16 cm. Shaping is not always to be preferred since it introduces some restriction in off-axis performance, which is detrimental for multibeam applications. Multiple beams for a large parabolic antenna can greatly increase sky coverage, which is particularly useful for survey observations. A beamformer feed system in which beams are formed using phased arrays of feed elements is described by Elmer et al. (2012), who consider various designs (see discussion in Sect. 5.7.2.1).

For tracking parabolic reflectors, there are numerous differences in the detailed design. For example, when a number of feeds for different frequency bands are required at the Cassegrain focus, these are sometimes mounted on a turntable structure, and the feed that is in use is brought to a position on the axis of the main reflector. Alternately, the feeds may be in fixed positions on a circle centered on the vertex, and by using a rotatable subreflector of slightly asymmetric design, the incoming radiation can be focused onto the required feed.

Parabolic reflector antennas with asymmetrical feed geometry can exhibit undesirable instrumental polarization effects that would largely cancel out in a circularly symmetrical antenna. This may occur in an unblocked aperture design, as in Fig. 5.1d, or in a design in which a cluster of feeds is used for operation on a number of frequency bands, where the feeds are close to, but not exactly on, the axis of the paraboloid. With crossed linearly polarized feeds, the asymmetry results in cross-polarization sidelobes within the main beam. With opposite circularly polarized feeds, the two beams are offset in opposite directions in a plane that is normal to the plane containing the axis of symmetry of the reflector and the center of the feed. This offset can be a serious problem in measurements of circular polarization, since the result is obtained by taking the difference between measurements with opposite circularly polarized responses (see Table 4.3). For measurements of linear polarization, the offset is less serious since this involves taking the product of two opposite-hand outputs, and the resulting response is symmetrical about the axis of

the parabola. The effects can be largely canceled by inserting a compensating offset in a secondary reflector. For further details, see Chu and Turrin (1973) and Rudge and Adatia (1978).

A basic point concerns the accuracy of the reflector surface. Deviations of the surface from the ideal profile result in variations in the phase of the electromagnetic field as it reaches the focus. We can think of the reflector surface as consisting of many small sections that deviate from the ideal surface by ϵ, a Gaussian random variable with probability distribution

$$p(\epsilon) = \frac{1}{\sqrt{2\pi}\,\sigma} e^{-\epsilon^2/2\sigma^2} \,, \tag{5.1}$$

where $\langle \epsilon \rangle = 0$, $\langle \epsilon^2 \rangle = \sigma^2$, and $\langle \ \rangle$ indicates the expectation. A relation of general importance in probabilistic calculations is $\langle e^{j\epsilon} \rangle$, which is

$$\langle e^{j\epsilon} \rangle = \int_{-\infty}^{\infty} p(\epsilon)e^{j\epsilon} d\epsilon = \frac{1}{\sqrt{2\pi}\sigma} \int_{-\infty}^{\infty} e^{-\frac{\epsilon^2}{2\sigma^2} - j\epsilon} \, d\epsilon = e^{-\sigma^2/2} \,. \tag{5.2}$$

The rightmost integral is accomplished by the method of completing the square in the argument of the exponential, i.e., $-\left(\frac{\epsilon^2}{2\sigma^2} + j\epsilon\right) = -\frac{1}{2\sigma^2}\left(\epsilon + j\sigma^2\right)^2 - \frac{\sigma^2}{2}$. The $e^{-\sigma^2/2}$ factor can be moved outside the integral, the rest of which is unity.

A surface deviation ϵ produces a deviation of approximately 2ϵ in the path length of a reflected ray; this approximation improves as the focal ratio is increased. Thus, a deviation ϵ causes a phase shift $\phi \simeq 4\pi\epsilon/\lambda$, where λ is the wavelength. As a result, the electric field components at the focus have a Gaussian phase distribution with $\sigma_\phi = 4\pi\sigma/\lambda$. If there are N independent sections of the surface, then the collecting area, which is proportional to the square of the electric field, is given by

$$A = A_0 \left\langle \left| \frac{1}{N} \sum_i e^{j\phi_i} \right|^2 \right\rangle = \frac{A_0}{N^2} \sum_{i,k} \langle e^{j(\phi_i - \phi_k)} \rangle \simeq A_0 e^{\frac{-\left(\sqrt{2}\sigma_\phi\right)^2}{2}}, \tag{5.3}$$

where A_0 is the collecting area for a perfect surface, and it has been assumed that N is large enough that terms for which $i = k$ can be ignored. The $\sqrt{2}$ factor comes from differencing two random variables. Then from Eqs. (5.2) and (5.3), we obtain

$$A = A_0 e^{-(4\pi\sigma/\lambda)^2} \,. \tag{5.4}$$

This equation is known in radio engineering as the Ruze formula (Ruze 1966) and in some other branches of astronomy as the Strehl ratio. As an example, if $\sigma/\lambda = 1/20$, the aperture efficiency, A/A_0, is 0.67. In the case of antennas with multiple reflecting surfaces, the rms deviations can be combined in the usual root-sum-squared manner. Secondary reflectors, such as a Cassegrain subreflector, are smaller than the main reflector, and for smaller surfaces, the rms deviation is usually correspondingly smaller. The surface adjustment of the 12-m-diameter antennas

of the Atacama Large Millimeter/submillimeter Array (ALMA) array, which are capable of operation up to ~ 900 GHz, is a good example of the accuracy that can be achieved (Mangum et al. 2006). A study of the dynamics of the surface of the antennas is described by Snel et al. (2007).

Several techniques have been developed for improving the performance of parabolic antennas. An example is the adjustment of the subreflector shape to compensate for errors in the main reflector [see, e.g., Ingalls et al. (1994), Mayer et al. (1994)]. Another improvement is in the design of the focal support structure to minimize blockage of the aperture and reduce sidelobes in the direction of the ground (Lawrence et al. 1994; Welch et al. 1996). A common method of supporting equipment near the reflector focus is the use of a tripod or quadrupod structure. If the legs of the structure are connected to the edge of the main reflector rather than to points within the reflector aperture, they interrupt only the plane wave incident on the aperture, not the spherical wavefront between the reflector and the focus. Use of an offset-feed reflector avoids any blockage of the incident wavefront in reaching the focus. However, both of these methods of reducing blockage increase the complexity and cost of the structure.

5.2 Sampling the Visibility Function

5.2.1 Sampling Theorem

The choice of configuration of the antennas of a synthesis array is largely based on optimizing the sampling of the visibility function in (u, v) space. Thus, in considering array design, it is logical to start by examining the sampling requirements. These are governed by the sampling theorem of Fourier transforms (Bracewell 1958). Consider first the measurement of the one-dimensional intensity distribution of a source, $I_1(l)$. It is necessary to measure the complex visibility $\mathcal{V}$ in the corresponding direction on the ground at a series of values of the projected antenna spacing. For example, to measure an east–west profile, a possible method is to make observations near meridian transit of the source using an east–west baseline and to vary the length of the baseline from day to day.

Figure 5.2a–c illustrates the sampling of the one-dimensional visibility function $\mathcal{V}(u)$. The sampling operation can be represented as multiplication of $\mathcal{V}(u)$ by the series of delta functions in Fig. 5.2b, which can be written

$$\left[\frac{1}{\Delta u}\right] \text{III}\left(\frac{u}{\Delta u}\right) = \sum_{i=-\infty}^{\infty} \delta(u - i\Delta u) , \tag{5.5}$$

where the left side is included to show how the series can be expressed in terms of the *shah function*, III, introduced by Bracewell and Roberts (1954). The series extends to infinity in both positive and negative directions, and the delta functions
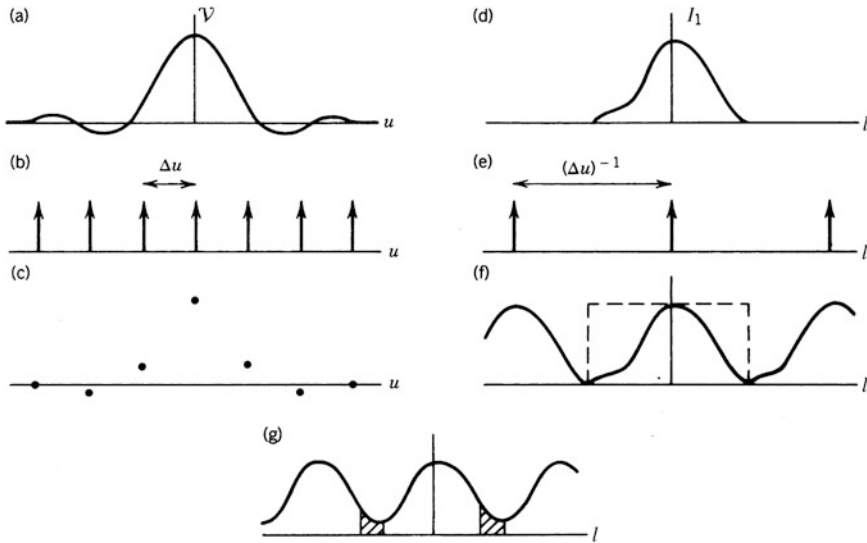
Fig. 5.2 Illustration of the sampling theorem: (**a**) visibility function $\mathcal{V}(u)$, real part only; (**b**) sampling function in which the arrows represent delta functions; (**c**) sampled visibility function; (**d**) intensity function $I_1(l)$; (**e**) replication function; (**f**) replicated intensity function. Functions in (**d**), (**e**), and (**f**) are the Fourier transforms of those in (**a**), (**b**), and (**c**), respectively. (**g**) is the replicated intensity function showing aliasing in the shaded areas resulting from using too large a sampling interval.

are uniformly spaced with an interval Δu. The Fourier transform of Eq. (5.5) is the series of delta functions shown in Fig. 5.2e:

$$\text{III}(l\Delta u) = \frac{1}{\Delta u} \sum_{p=-\infty}^{\infty} \delta\left(l - \frac{p}{\Delta u}\right) . \tag{5.6}$$

In the l domain, the Fourier transform of the sampled visibility is the convolution of the Fourier transform of $\mathcal{V}(u)$, which is the one-dimensional intensity function $I_1(l)$, with Eq. (5.6). The result is the replication of $I_1(l)$ at intervals $(\Delta u)^{-1}$ shown in Fig. 5.2f. If $I_1(l)$ represents a source of finite dimensions, the replications of $I_1(l)$ will not overlap as long as $I_1(l)$ is nonzero only within a range of l that is no greater than $(\Delta u)^{-1}$. Hence, if l_w is the range over which $I_1(l)$ is nonzero or, more generally, the field of view of an observation, then the avoidance of aliasing requires $\Delta u \leq 1/l_w$. An example of overlapping replications is shown in Fig. 5.2g. The loss of information resulting from such overlapping is commonly referred to as *aliasing*, because the components of the function within the overlapping region lose their identity with respect to which end of the replicated function they properly belong. The distortion in the replicated intensity function is said to be caused by "leakage" [see Bracewell (2000)].

The requirement for the restoration of a function from a set of samples, for example, deriving the function in Fig. 5.2a from the samples in Fig. 5.2c, is easily understood by considering the Fourier transforms in Fig. 5.2d and f. Interpolation in the u domain corresponds to removing the replications in the l domain, which can be achieved by multiplying the function in Fig. 5.2f by the rectangular function indicated by the broken line. In the u domain, this multiplication corresponds to convolution of the sampled values with the Fourier transform of the rectangular function, which is the unit area sinc function,

$$\frac{\sin \pi u / \Delta u}{\pi u} \ . \tag{5.7}$$

If aliasing is avoided, convolution with (5.7) provides exact interpolation of the original function from the samples. Note that perfect restoration requires a sum over all samples except when the sinc function is centered on a specific sample. Thus, we can state, as the sampling theorem for the visibility, that *if the intensity distribution is nonzero only within an interval of width l_w, $I_1(l)$ is fully specified by sampling the visibility function at points spaced $\Delta u = l_w^{-1}$ in u.* The interval $\Delta u = l_w^{-1}$ is called the critical sampling interval. Sampling at a finer interval in u is called oversampling and usually does no harm nor does it provide any benefit. Sampling at a coarser interval is called undersampling, which leads to aliasing.

Aliasing can lead to serious misinterpretation of source structure. For example, suppose the intensity function $I_1(l)$ consists of a number of compact separated components. A component that lies outside the proper sampling window, i.e., $|l| > l_w/2$, at negative l will be aliased to a position on the positive side of the replicated intensity function. Thus, its appears at the wrong position. This error can be discovered by regridding the data at a finer interval Δu. An aliased component will move in an unexpected way in the image plane.

The spatial sampling theorem described here is just a formulation of the standard Shannon–Nyquist theorem normally written in the time (t)-frequency (ν) domain. Here, the critical sampling frequency for a temporal waveform of bandwidth $\Delta \nu$ is $1/(2\Delta \nu)$. The factor of two appears because the spectrum in Fourier space extends from $-\Delta \nu$ to $+\Delta \nu$.

In two dimensions, it is simply necessary to apply the theorem separately to the source in the l and m directions. A compact source that is just beyond the sampling limit at the lower left of the image will be aliased into the sampling interval in the upper right. For further discussion of the sampling theorem, see, for example, Unser (2000).

5.2.2   Discrete Two-Dimensional Fourier Transform

The derivation of an image (or map) from the visibility measurements is the subject of Chap. 10, but it is important at this point to understand the form

in which the visibility data are required for this transformation. The discrete Fourier transform (DFT) is very widely used in synthesis imaging because of the computational advantages of the fast Fourier transform (FFT) algorithm [see, e.g., Brigham (1988)]. The basic properties of the DFT in one dimension are described in Appendix 8.4. In two dimensions, the functions $\mathcal{V}(u, v)$ and $I(l, m)$ are expressed as rectangular matrices of sampled values at uniform increments in the two variables involved. The rectangular grid points on which the intensity is obtained provide a convenient form for further data processing.

The two-dimensional form of the discrete transform for a Fourier pair f and g is defined by

$$f(p,q) = \sum_{i=0}^{M-1} \sum_{k=0}^{N-1} g(i,k)\, e^{-j2\pi ip/M} e^{-j2\pi kq/N} \ , \tag{5.8}$$

and the inverse is

$$g(i,k) = \sum_{p=0}^{M-1} \sum_{q=0}^{N-1} f(p,q)\, e^{j2\pi ip/M} e^{j2\pi kq/N} \ . \tag{5.9}$$

The functions are periodic with periods of M samples in the i and p dimensions and N samples in the k and q dimensions. Evaluation of Eqs. (5.8) or (5.9) by direct computation requires approximately $(MN)^2$ complex multiplications. In contrast, if M and N are powers of 2, the FFT algorithm requires only $\frac{1}{2}MN \log_2(MN)$ complex multiplications.

The transformation between $\mathcal{V}(u, v)$ and $I(l, m)$, where I is the source intensity in two dimensions, is obtained by substituting $g(i,k) = I(i\Delta l, k\Delta m)$ and $f(p,q) = \mathcal{V}(p\Delta u, q\Delta v)$ in Eqs. (5.8) and (5.9). The relationship between the integral and discrete forms of the Fourier transform is found in several texts; see, for example, Rabiner and Gold (1975) or Papoulis (1977). The dimensions of the (u, v) plane that contain these data are $M\Delta u$ by $N\Delta v$. In the (l, m) plane, the points are spaced Δl in l and Δm in m, and the image dimensions are $M\Delta l$ by $N\Delta m$. The dimensions in the two domains are related by

$$\Delta u = (M\Delta l)^{-1}, \qquad \Delta v = (N\Delta m)^{-1} \ ,$$
$$\Delta l = (M\Delta u)^{-1}, \qquad \Delta m = (N\Delta v)^{-1} \ . \tag{5.10}$$

The spacing between points in one domain is the reciprocal of the total dimension in the other domain. Thus, if the size of the array in the intensity domain is chosen to be large enough that the intensity function is nonzero only within the area $M\Delta l \times N\Delta m$, then the spacings Δu and Δv in Eq. (5.10) satisfy the sampling theorem.
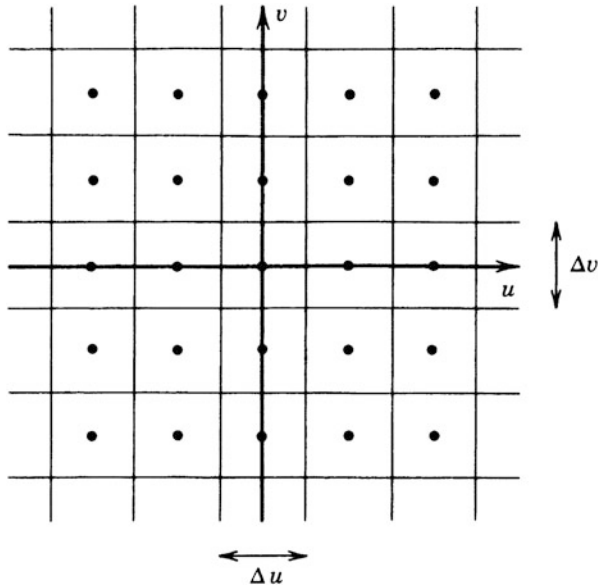
Fig. 5.3 Points on a rectangular grid in the (u, v) plane at which the visibility is sampled for use with the discrete Fourier transform. As shown, the spacings Δu and Δv are equal. The division of the plane into grid cells of size $\Delta u \times \Delta v$ is also shown.

To apply the discrete transform to synthesis imaging, it is necessary to obtain values of $\mathcal{V}(u, v)$ at points separated by Δu in u and by Δv in v, as shown in Fig. 5.3. However, the measurements are generally not made at (u, v) points on a grid since for tracking interferometers, they fall on elliptical loci in the (u, v) plane, as explained in Sect. 4.1. Thus, it is necessary to obtain the values at the grid points by interpolation or similar processes. In Fig. 5.3, the plane is divided into cells of size $\Delta u \times \Delta v$ centered on the grid points. A very simple method of determining a visibility value to assign at each grid point is to take the mean of all values that fall within the same cell. This procedure has been termed *cell averaging* (Thompson and Bracewell 1974). Better procedures are generally used; see Sect. 10.2.2. However, the cell averaging concept helps one to visualize the required distribution of the measurements; ideally there should be at least one measurement, or a small number of measurements, within each cell. Thus, the baselines should be chosen so that the spacings between the (u, v) loci are no greater than the cell size, to maximize the number of cells that are intersected by a locus. Cells that contain no measurements result in holes in the (u, v) coverage, and minimization of such holes is an important criterion in array design. Lobanov (2003) and Lal et al. (2009) discuss the performance of arrays based on uniformity of (u, v) coverage (see Sect. 5.4.2).

## 5.3   Introductory Discussion of Arrays

5.3.1   Phased Arrays and Correlator Arrays

An array of antennas can be interconnected to operate as a phased array or as a correlator array. Figure 5.4a shows a simple schematic diagram of a phased array connected to a square-law detector, in which the number of antennas, n_a, is equal to four. If the voltages at the antenna outputs are V_1, V_2, V_3, and so on, the output of the square-law detector is proportional to

$$(V_1 + V_2 + V_3 + \cdots + V_{n_a})^2 . \tag{5.11}$$

Note that for n_a antennas, there are $n_a(n_a - 1)$ cross-product terms of form $V_m V_n$ involving different antennas m and n, and n_a self-product terms of form V_m^2. If the

Fig. 5.4 Simple four-element linear array. ℓ_λ is the unit antenna spacing measured in wavelengths, and θ indicates the angle of incidence of a signal. (**a**) Connected as a phased array with an adjustable phase shifter in the output of each antenna, and the combined signal applied to a square-law detector. The voltage combiner is a matching network in which the output is proportional to the sum of the radio-frequency input voltages. (**b**) The same antennas connected as a correlator array. (**c**) The ordinate is the response of the array: the scale at the left applies to the phased array, and at the right to the correlator array. The abscissa is proportional to θ in units of ℓ_λ^{-1} rad. The equal spacing between antennas in this simple grating array gives rise to sidelobes in the form of replications of the central beam.
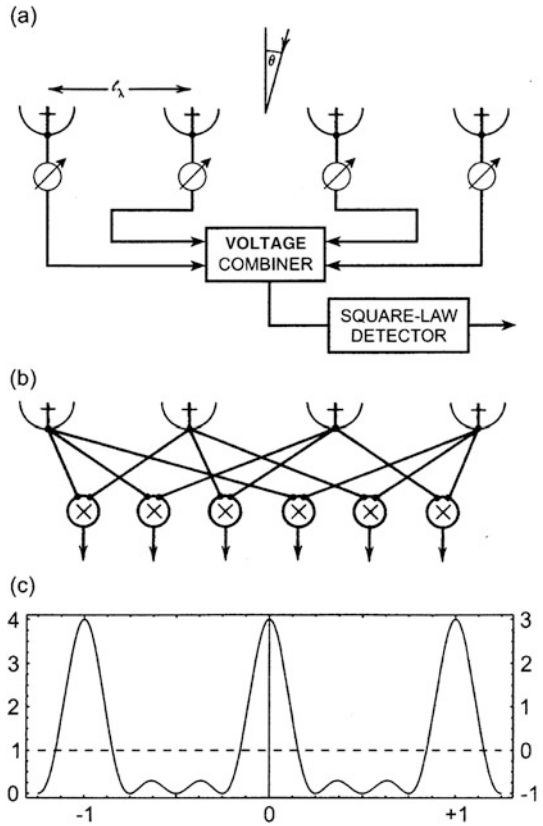
signal path (including the phase shifter) from each antenna to the detector is of
the same electrical length, the signals combine in phase when the direction of the
incoming radiation is given by

$$\theta = \sin^{-1}\left(\frac{N}{\ell_\lambda}\right) , \tag{5.12}$$

where N is an integer, including zero, and ℓ_λ is the spacing interval measured in
wavelengths. The position angles of the maxima, which represent the beam pattern
of the array, can be varied by adjusting the phase shifters at the antenna outputs.
Thus, the beam pattern can be controlled and, for example, scanned to form an
image of an area of sky.

In correlator arrays, a correlator generates the cross product of the signal voltages
$V_m V_n$ for every antenna pair, as in Fig. 5.4b. These outputs take the form of
fringe patterns and can be combined to produce maxima similar to those of the
phased array. If a phase shift is introduced at the output of one of the correlator
array antennas, the result appears as a corresponding change in the phase of
the fringes measured with the correlator connected to that antenna. Conversely,
the effect of an antenna phase shift can be simulated by changing the measured
phases when combining the correlator outputs. Thus, a beam-scanning action can
be accomplished by combining measured cross-correlations in a computer with
appropriate variations in the phase. This is what happens in computing the Fourier
transform of the visibility function, that is, the Fourier transform of the correlator
outputs as a function of spacing. The loss of the self-product terms reduces the
instantaneous sensitivity of the correlator array by a factor $(n_a - 1)/n_a$ in power,
which is close to unity if n_a is large. However, at any instant, the correlator array
responds to the whole field of the individual antennas, whereas the response of the
phased array is determined by the narrow beam that it forms, unless it is equipped
with a more complex signal-combining network that allows many beams to be
formed simultaneously. Thus, in imaging, the correlator array gathers data more
efficiently than the phased array.

The response pattern of the correlator array to a point source is the same as
that of the phased array, except for the self-product terms. The response of the
phased array consists of one or more beams in the direction in which the antenna
responses combine with equal phase. These are surrounded by sidelobes, the pattern
and magnitude of which depend on the number and configuration of antennas.
Between individual sidelobe peaks, there will be nulls that can be as low as zero,
but the response is positive because the output of the square-law detector cannot go
negative. Now consider subtracting the self-product terms, to simulate the response
of the correlator array. Over a field of view small compared with the beamwidth
of an individual antenna, each self-product term represents a constant level, and
each cross product represents a fringe oscillation. In the response to a point source,
all of these terms are of equal magnitude. Subtracting the self-products from the

phased-array response causes the zero level to be shifted in the positive direction by an amount equal to $1/n_a$ of the peak level, as indicated by the broken line in Fig. 5.4c. The points that represent zeros in the phased-array response become the peaks of negative sidelobes. Thus, in the response of the correlator array, the positive values are decreased by a factor $(n_a - 1)/n_a$ relative to those of the phased array. In the negative direction, the response extends to a level of $-1/(n_a - 1)$ of the positive peak but no further since this level corresponds to the zero level of the phased array. Kogan (1999) pointed out this limitation on the magnitude of the negative sidelobes of a correlator array and also noted that this limit depends not on the configuration of the individual antennas but only on their number. Neither of these conclusions applies to the positive sidelobes. This result is strictly true only for snapshot observations [i.e., those in which the (u, v) coverage is not significantly increased by Earth rotation] and for uniform weighting of the correlator outputs.

Finally, consider some characteristics of a phased array as in Fig. 5.4a. The power combiner is a passive network, for example, the branched transmission line in Fig. 1.13a. If a *correlated* waveform of power P is applied to each combiner input, then the output power is $n_a P$. In terms of the voltage V at each input, a fraction $1/\sqrt{n_a}$ of each *voltage* combines additively to produce an output of $\sqrt{n_a} V$, or $n_a P$ in power. Now if the input waveforms are *uncorrelated*, again each contributes $V/\sqrt{n_a}$ in voltage but the resulting *powers* combine additively (i.e., as the sum of the squared voltages), so in this case, the power at the output is equal to the power P at one input. Each input then contributes only $1/n_a$ of its power to the output, and the remaining power is dissipated in the terminating impedances of the combiner inputs (i.e., radiated from the antennas if they are directly connected to the combiner). The signals from an unresolved source received in the main beam of the array are fully correlated, but the noise contributions from amplifiers at the antennas are uncorrelated. Thus, if there are no losses in the transmission lines or the combiner, the same signal-to-noise ratio at the detector is obtained by inserting an amplifier at the output of each antenna, or a single amplifier at the output of the combiner. However, such losses are often significant, so generally it is advantageous to use amplifiers at the antennas. Note that if half of the antennas in a phased array are pointed at a radio source and the others at blank sky, the signal power at the combiner output is one-quarter of that with all antennas pointed at the source.

5.3.2   Spatial Sensitivity and the Spatial Transfer Function

We now consider the sensitivity of an antenna or array to the spatial frequencies on the sky. The angular response pattern of an antenna is the same in reception or transmission, and at this point it may be easier to consider the antenna in transmission. Then power applied to the terminals produces a field at the antenna aperture. A function $W(u, v)$ is equal to the autocorrelation function of the distribution of the electric field across the aperture, $\mathcal{E}(x_\lambda, y_\lambda)$. Here x_λ and y_λ are coordinates in the

aperture plane of the antenna and are measured in wavelengths. Thus,

$$W(u, v) = \mathcal{E}(x_\lambda, y_\lambda) \star\star \mathcal{E}^*(x_\lambda, y_\lambda)$$

$$= \int_{-\infty}^{\infty} \int_{-\infty}^{\infty} \mathcal{E}(x_\lambda, y_\lambda)\, \mathcal{E}^*(x_\lambda - u, y_\lambda - v)\, dx_\lambda \, dy_\lambda \;. \tag{5.13}$$

The double-pentagram symbol represents two-dimensional autocorrelation. The integral in Eq. (5.13) is proportional to the number of ways, suitably weighted by the field intensity, in which a specific spacing vector (u, v) can be found within the antenna aperture. In reception, $W(u, v)$ is a measure of the sensitivity of the antenna to different spatial frequencies. In effect, the antenna or array acts as a spatial frequency filter, and $W(u, v)$ is widely referred to as the *transfer function* by analogy with the usage of this term in filter theory. $W(u, v)$ has also been called the spectral sensitivity function (Bracewell 1961, 1962), which refers to the spectrum of spatial frequencies (not the radio frequencies) to which the array responds. We use the terms *spatial transfer function* and *spatial sensitivity* when discussing $W(u, v)$. The area of the (u, v) plane over which measurements can be made [i.e., the support of $W(u, v)$, defined as the closure of the domain within which $W(u, v)$ is nonzero] is referred to as the *spatial frequency coverage*, or the (u, v) coverage.

Consider the response of the antenna or array to a point source. Since the visibility of a point source is constant over the (u, v) plane, the measured spatial frequencies are proportional to $W(u, v)$. Thus, the point-source response $\mathcal{A}(l, m)$ is the Fourier transform of $W(u, v)$. This result is formally derived by Bracewell and Roberts (1954). [Recall from the discussion preceding Eq. (2.15) that the point-source response is the mirror image of the antenna power pattern: $\mathcal{A}(l, m) = A(-l, -m)$.] The spatial transfer function $W(u, v)$ is an important feature in this chapter, and Fig. 5.5 further illustrates its place in the interrelationships between functions involved in radio imaging.

Figure 5.6a shows an interferometer in which the antennas do not track and are represented by two rectangular areas. We shall assume that $\mathcal{E}(x_\lambda, y_\lambda)$ is uniformly distributed over the apertures, such as in the case of arrays of uniformly excited dipoles. First suppose that the output voltages from the two apertures are summed and fed to a power-measuring receiver, as in some early instruments. The three rectangular areas in Fig. 5.6b represent the autocorrelation function of the aperture distributions, that is, the spatial transfer function. Note that the autocorrelation of the two apertures contains the autocorrelation of the individual apertures (the central rectangle in Fig. 5.6b) plus the cross-correlation of the two apertures (the shaded rectangles). If the two antennas are combined using a correlator instead of a receiver that responds to the total received power, the spatial sensitivity is represented by only the shaded rectangles since the correlator forms only the cross products of signals from the two apertures.

The interpretation of the spatial transfer function as the Fourier transform of the point-source response can be applied to both the adding and correlator cases. For example, for the correlator implementation of the interferometer in Fig. 5.6a, the
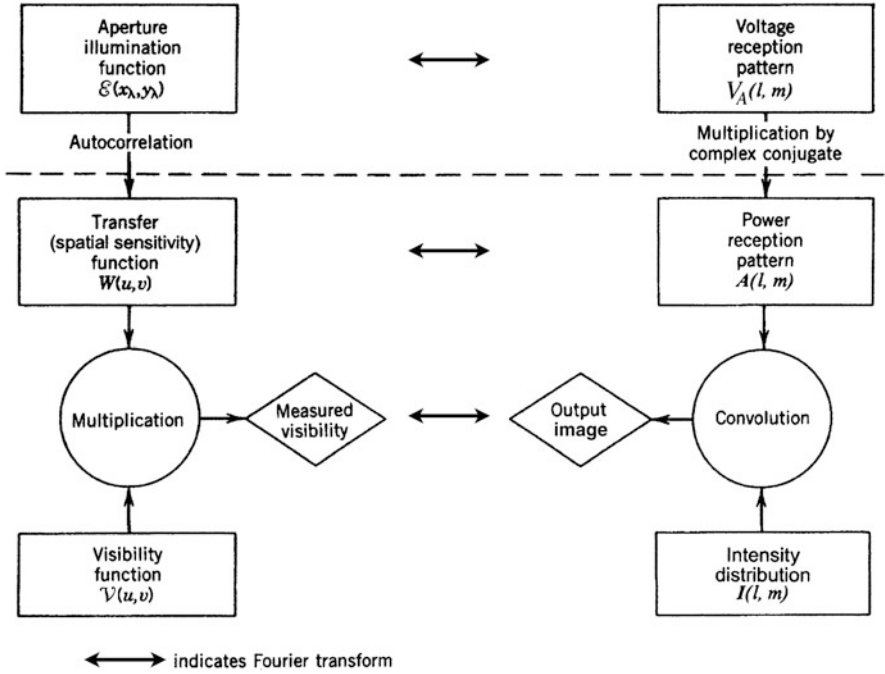
Fig. 5.5 Relationships between functions involved in imaging a source. Starting at the top left, the autocorrelation of the aperture distribution of the electric field over an antenna $\mathcal{E}(x_\lambda, y_\lambda)$ gives the spatial transfer function $W(u, v)$. The measured visibility in the observation of a source is the product of the source visibility $\mathcal{V}(u, v)$ and the spatial transfer function. At the top right, the multiplication of the voltage reception pattern $V_A(l, m)$ with its complex conjugate produces the power reception pattern $A(l, m)$. Imaging of the source intensity distribution $I(l, m)$ results in convolution of this function with the antenna power pattern. The Fourier transform relationships between the quantities in the (x_λ, y_λ) and (u, v) domains, and those in the (l, m) domain, are indicated by the bidirectional arrows. When the spatial sensitivity is built up by Earth rotation, as in tracking arrays, it cannot, in general, be described as the autocorrelation function of any field distribution. Only the part of the diagram below the broken line applies in such cases.

response to a point source is the Fourier transform of the function represented by the shaded areas. This Fourier transform is

$$\left[\frac{\sin \pi x_{\lambda 1} l}{\pi x_{\lambda 1} l} \right]^2 \left[\frac{\sin \pi y_{\lambda 1} m}{\pi y_{\lambda 1} m} \right]^2 \cos 2\pi D_\lambda l \,, \tag{5.14}$$

where $x_{\lambda 1}$ and $y_{\lambda 1}$ are the aperture dimensions, and D_λ is the aperture separation, all measured in wavelengths. The sinc-squared functions in (5.14) represent the power pattern of the uniformly illuminated rectangular apertures, and the cosine term represents the fringe pattern. In early instruments, the relative magnitude of the spatial sensitivity was controlled only by the field distribution over the antennas, but image processing by computer enables the magnitude to be adjusted after an observation has been made.
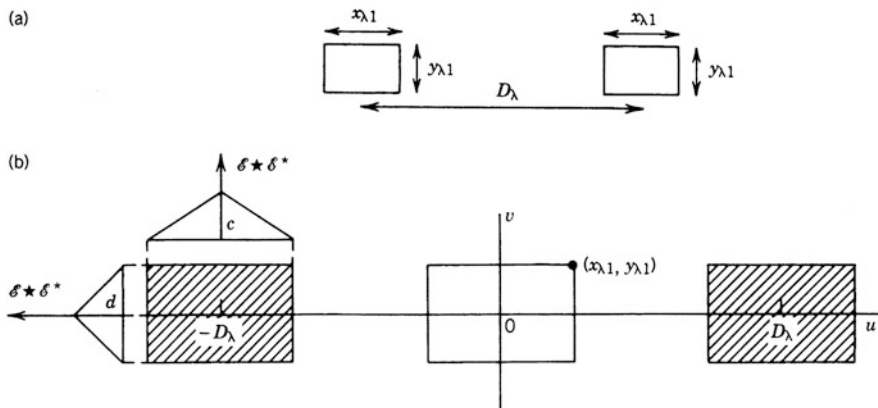
Fig. 5.6 The two apertures in (**a**) represent a two-element interferometer, the spatial transfer function of which is shown in (**b**). The shaded areas contain the spatial sensitivity components that result from the cross-correlation of the signals from the two antennas. If the field distribution is uniform over the apertures, the magnitude of the spatial sensitivity is linearly tapered. This is indicated by c and d, which represent cross sections of the spatial transfer function.

Some commonly used configurations of antenna arrays, and the boundaries of their autocorrelation functions, are shown in Fig. 5.7. The autocorrelation functions indicate the instantaneous spatial sensitivity for a continuous aperture in the form of the corresponding figure. Equation (5.13) shows that the autocorrelation function is the integral of the product of the field distribution with its complex conjugate displaced by u and v. By investigating the values of u and v for which the two aperture figures overlap, it is easy to determine the boundary within which the spatial transfer function is nonzero, using graphical procedures described by Bracewell (1961, 1995). It is also possible to identify ridges of high autocorrelation that occur for displacements at which the arms of figures such as those in Fig. 5.7a, b, or c are aligned. In the case of the ring, Fig. 5.7g, the autocorrelation function is proportional to the area of overlap at the two points where the ring intersects with its displaced replication. This area decreases monotonically for a ring of unit diameter until $q = \sqrt{u^2 + v^2} = 1/\sqrt{2}$, where the tangents to the two rings at the intersection points are $\pi/2$. For $q > 1/\sqrt{2}$, the autocorrelation function increases as the tangents realign. The analytic form of the autocorrelation function, shown in Fig. 5.7j, is the Fourier transform of a J_0^2 Bessel function, which is proportional to $1/(q\sqrt{1-q^2})$, for $0 \leq q \leq 1$. Another interesting aperture is a filled circle, for which the autocorrelation function decreases monotonically from $q = 0$ to 1 with the form $\cos^{-1}(q) - q\sqrt{1-q^2}$, which Bracewell (2000) calls the Chinese hat function. When the aperture is not completely filled, that is, when the figure represents an array of discrete antennas, the spatial sensitivity takes the form of samples of the autocorrelation function. For example, for a cross of uniformly spaced antennas, the square in Fig. 5.7b would be represented by a matrix pattern within the square boundary.

Fig. 5.7 Configurations for array apertures and the boundaries within which the corresponding autocorrelation functions are nonzero. The configurations represent the aperture (x_λ, y_λ) plane and the autocorrelations, the spatial frequency (u, v) plane. (**a**) The cross and (**b**) its autocorrelation boundary. (**c**) The T-shaped array and (**d**) its autocorrelation boundary. (**e**) The equiangular Y-shaped array and (**f**) its autocorrelation boundary. The broken lines in (**b**), (**d**), and (**f**) indicate ridges of high autocorrelation value. (**g**) The ring and (**h**) its autocorrelation boundary. The autocorrelation function of the ring is circularly symmetrical and (**j**) shows the radial profile of the function from the center to the edge of the circle in (**h**). (**i**) The Reuleaux triangle. The broken lines indicate an equilateral triangle, and the circular arcs that form the Reuleaux triangle have radii centered on the vertices of the triangle. The autocorrelation of the Reuleaux triangle is bounded by the same circle shown in (**h**) but does not have the same autocorrelation function as the ring.
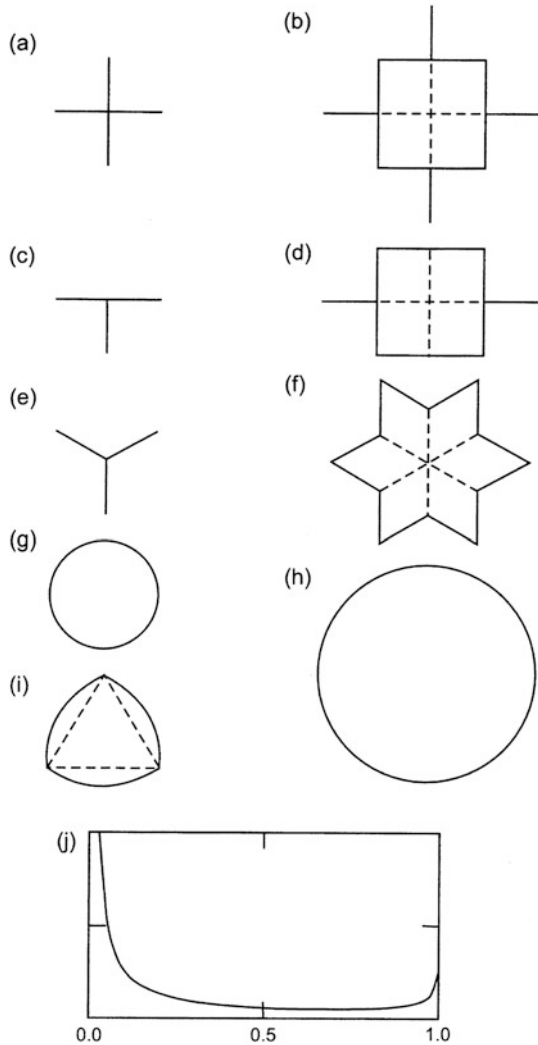
5.3.3 Meter-Wavelength Cross and T-Shaped Arrays

A cross and its autocorrelation function are shown in Fig. 5.7a and b. It is assumed that the width of the arms is finite but small compared with the length of the arms. In the case of the Mills cross (Mills 1963) described briefly in Chap. 1, the outputs of the two arms go to a single cross-correlating receiver, so the spatial sensitivity is represented by the square in Fig. 5.7b. The narrow extensions on the centers of the

sides of the square represent parts of the autocorrelation functions of the individual arms, which are not formed in the cross-correlation of the arms. However, they are formed if the arms consist of lines of individual antennas, for which the cross-correlation is formed for pairs on the same arm as well as those on crossed arms. The case for a T-shaped array is similar and is shown in Fig. 5.7c and d.

If the sensitivity (i.e., the collecting area per unit length) is uniform along the arms for a cross or a corresponding T, then the weighting of the spatial sensitivity is uniform over the square (u, v) area; note that it does not taper linearly from the center as in the situation in Fig. 5.6. At the edge of the square area, the spatial sensitivity falls to zero in a distance equal to the width of the arms. Such a sharp edge, resulting from the uniform sensitivity, results in strong sidelobes. Therefore, an important feature of the Mills cross design was a Gaussian taper of the coupling of the elements along the arms to reduce the sensitivity to about 10% at the ends. This greatly reduced local maxima in the response resulting from sidelobes outside the main beam, at the expense of some broadening of the beam.

Figure 1.12a shows an implementation of a T-shaped array that is an example of a nontracking correlator interferometer. Here, a small antenna is moved in steps, with continuous coverage, to simulate a larger aperture; see Blythe (1957), Ryle et al. (1959), and Ryle and Hewish (1960). The spatial frequency coverage is the same as would be obtained in a single observation with an antenna of aperture equal to that simulated by the movement of the small antenna, although the magnitude of the spatial sensitivity is not exactly the same. The term *aperture synthesis* was introduced to describe such observations, but to be precise, it is the *autocorrelation* of the aperture that is synthesized (see Sect. 5.4).

5.4 Spatial Transfer Function of a Tracking Array

The range of spatial frequencies that contribute to the output of an interferometer with tracking antennas is illustrated in Fig. 5.8b. The two shaded areas represent the cross-correlation of the two apertures of an east–west interferometer for a source on the meridian. As the source moves in hour angle, the changing (u, v) coverage is represented by a band centered on the spacing locus of the two antennas. Recall from Sect. 4.1 that the locus for an Earth-based interferometer is an arc of an ellipse, and that since $\mathcal{V}(-u, -v) = \mathcal{V}^*(u, v)$, any pair of antennas measures visibility along two arcs symmetric about the (u, v) origin, both of which are included in the spatial transfer function.

Because the antennas track the source, the antenna beams remain centered on the same point in the source under investigation, and the array measures the product of the source intensity distribution and the antenna pattern. Another view of this effect is obtained by considering the radiation received by small areas of the apertures of two antennas, the centers of which are A_1 and A_2 in Fig. 5.9. The antenna apertures encompass a range of spacings from $u - d_\lambda$ to $u + d_\lambda$ wavelengths, where d_λ is the antenna diameter measured in wavelengths. If the antenna beams remain

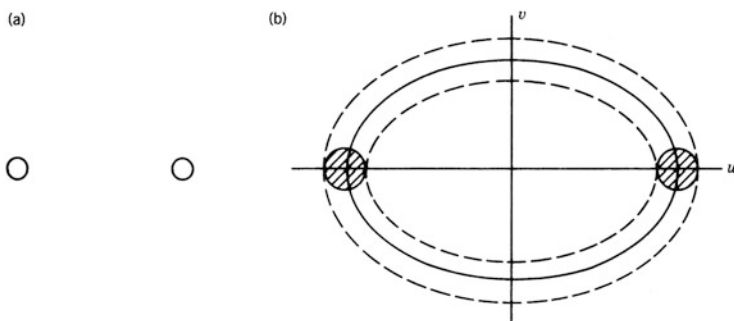**Fig. 5.8** (**a**) The aperture of an east–west, two-element interferometer. The corresponding spatial frequency coverage for cross-correlated signals is shown by the shaded areas in (**b**). If the antennas track the source, the spacing vector traces out an elliptical locus (the solid line) in the (u, v) plane. The area between the broken lines in (**b**) indicates the spatial frequencies that contribute to the measured values. The spacing between the broken lines is determined by the cross-correlation of the antenna aperture.
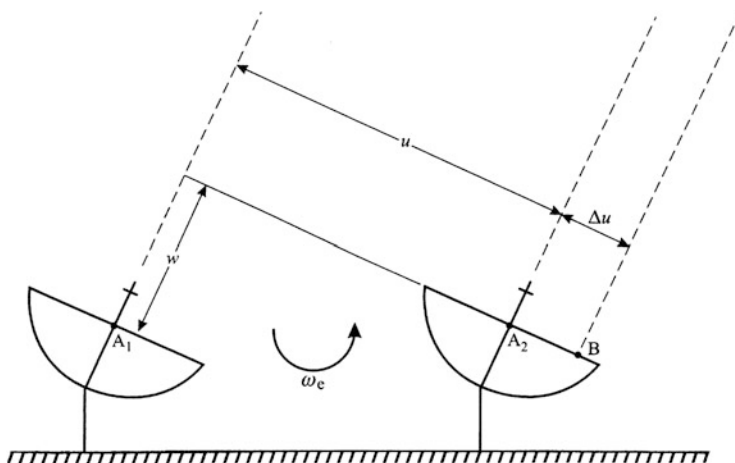

Fig. 5.9 Illustration of the effect of tracking on the fringe frequency at the correlator output. The u component of the baseline is shown, and the v component is omitted since it does not affect the fringe frequency. The curved arrow indicates the tracking motion of the antennas.

fixed in position as a source moves through them, then the correlator output is a combination of fringe components with frequencies from $\omega_e(u - d_\lambda) \cos \delta$ to $\omega_e(u+d_\lambda) \cos \delta$, where ω_e is the angular velocity of the Earth and δ is the declination of the source. To examine the effect when the antennas track the source, consider the point B, which, because of the tracking, has a component of motion toward the source equal to $\omega_e \Delta u \cos \delta$ wavelengths per second. This causes a corresponding Doppler shift in the signal received at B. To obtain the fringe frequency for waves arriving at A_1 and B, we subtract the Doppler shift from the nontracking fringe

frequency and obtain $[\omega_e(u + \Delta u)\cos\delta] - (\omega_e \Delta u \cos\delta) = (\omega_e u \cos\delta)$. The fringe frequency when tracking is thus the same as for the central points A_1 and A_2 of the apertures. (This is true for any pair of points; choosing one point at an antenna center in the example above slightly simplifies the discussion.) Thus, if the antennas track, the contributions from all pairs of points within the apertures appear at the same fringe frequency at the correlator output. As a result, such contributions cannot be separated by Fourier analysis of the correlator output waveform, and information on how the visibility varies over the range $u - d_\lambda$ to $u + d_\lambda$ is lost. However, if the antenna motion differs from a purely tracking one, the information is, in principle, recoverable. In imaging sources wider than the antenna beams, an additional scanning motion to cover the source is added to the tracking motion. In effect, this scanning allows the visibility to be sampled at intervals in u and v that are fine enough for the extended width of the source. This technique, known as *mosaicking*, is described in Sect. 11.5.

To accommodate the effects that result when the antennas track the source position, the normalized antenna pattern is treated as a modification to the intensity distribution, which then becomes $A_N(l, m)I(l, m)$. The spatial transfer function $W(u, v)$ for a pair of tracking antennas is represented at any instant by a pair of two-dimensional delta functions $^2\delta(u, v)$ and $^2\delta(-u, -v)$. For an array of antennas, the resulting spatial transfer function is represented by a series of delta functions weighted in proportion to the magnitude of the instrumental response. As the Earth rotates, these delta functions generate the ensemble of elliptical spacing loci. The loci represent the spatial transfer function of a tracking array.

Consider observation of a source $I(l, m)$, for which the visibility function is $\mathcal{V}(u, v)$, with normalized antenna patterns $A_N(l, m)$. Then if $W(u, v)$ is the spatial transfer function, the measured visibility is

$$\left[\mathcal{V}(u, v) * * \overline{A}_N(u, v)\right] W(u, v) \,, \tag{5.15}$$

where the double asterisk indicates two-dimensional convolution and the bar denotes the Fourier transform. The Fourier transform of (5.15) gives the measured intensity:

$$[I(l, m)A_N(l, m)] * * \overline{W}(l, m) \,. \tag{5.16}$$

If we observe a point source at the (l, m) origin, where $A_N = 1$, expression (5.16) becomes the point-source response $b_0(l, m)$. We then obtain

$$b_0(l, m) = \left[^2\delta(l, m)A_N(l, m)\right] * * \overline{W}(l, m) = \overline{W}(l, m) \,, \tag{5.17}$$

where the two-dimensional delta function, $^2\delta(l, m)$, represents the point source. Here again, the point-source response is the Fourier transform of the spatial transfer function. In the tracking case, the spatial frequencies that contribute to the measurement are represented by $W(u, v) * * \overline{A}_N(u, v)$. Note that $\overline{A}_N(u, v)$ is twice as wide as the corresponding antenna aperture in the (x, y) domain.

The term *aperture synthesis* is sometimes extended to include observations that involve hour-angle tracking. However, it is not possible to define an exactly equivalent antenna aperture for a tracking array. For example, consider the case of two antennas with an east–west baseline tracking a source for a period of 12 h. The spatial transfer function is an ellipse centered on the origin of the (u, v) plane, with zero sensitivity within the ellipse (except for a point at the origin that could be supplied by a measurement of total power received in the antennas). The equivalent aperture would be a function, the autocorrelation of which is the same elliptical ring as the spatial transfer function. No such aperture function exists, and thus the term "aperture synthesis" can only loosely be applied to describe most observations that include hour-angle tracking.

5.4.1   Desirable Characteristics of the Spatial Transfer Function

As a first step in considering the layout of the antennas, it is useful to consider the desired spatial (u, v) coverage [see, e.g., Keto (1997)]. For any specific observation, the optimum (u, v) coverage clearly depends on the expected intensity distribution of the source under study, since one would prefer to concentrate the capacity of the instrument in (u, v) regions where the visibility is nonzero. However, most large arrays are used for a wide range of astronomical objects, so some compromise approach is required. Since, in general, astronomical objects are aligned at random in the sky, there is no preferred direction for the highest resolution. Thus, it is logical to aim for visibility measurements that extend over a circular area centered on the (u, v) origin.

As described in Sect. 5.2.2, the visibility data may be interpolated onto a rectangular grid for convenience in Fourier transformation, and if approximately equal numbers of measurements are used for each grid point, they can be given equal weights in the transformation. Uneven weighting results in loss of sensitivity, since some values then contain a larger component of noise than others. From this viewpoint, one would like the natural weighting (i.e., the weighting of the measurements that results from the array configuration without further adjustment) to be as uniform as possible within the circular area.

For a general-purpose array, it is difficult to improve on the circularity of the measurement area. However, there are exceptions to the uniformity of the measurements within the circle. As mentioned above, in the Mills cross, uniform coupling of the radiating elements along the arms would result in uniform spatial sensitivity. To reduce sidelobes, a Gaussian taper of the coupling was introduced, resulting in a similar taper in the spatial sensitivity. This was particularly important because at the frequencies for which this type of instrument was constructed, typically in the range 85–408 MHz, source confusion can be a serious problem. Sidelobe responses can be mistaken for sources and can also mask genuine sources.

For a spatial sensitivity function of uniform rectangular character, the beam has a sinc function $(\sin \pi x / \pi x)$ profile, for which the first sidelobe has a relative strength of 0.217. For a uniform, circular, spatial transfer function, the beam has a profile of the form $J_1(\pi x)/\pi x$ for which the first sidelobe has a relative strength of 0.132. Sidelobes for a uniform circular (u, v) coverage are less than for a rectangular one but would still be a problem in conditions of source confusion. Tapering of the antenna illumination reduces the sidelobe responses. Thus, the uniform weighting may not be optimum for conditions of high source density.

5.4.2 Holes in the Spatial Frequency Coverage

Consider a circular (u, v) area of diameter a_λ wavelengths in which there are no holes in the data; that is, the visibility data interpolated onto a rectangular grid for Fourier transformation has no missing values. Then for uniform weighting, the synthesized beam, which is obtained from the Fourier transform of the gridded transfer function, has the form $J_1(\pi a_\lambda \theta)/\pi a_\lambda \theta$, where θ is the angle measured from the beam center. If centrally concentrated weighting is used, the beam is a smoothed form of this function. Let us refer to the (u, v) area described above as the complete (u, v) coverage and the resulting beam as the complete response. Now if some data are missing, the actual (u, v) coverage is equal to the complete coverage minus the (u, v) hole distribution. By the additive property of Fourier transforms, the corresponding synthesized beam is equal to the complete response minus the Fourier transform of the hole distribution. The holes result in an unwanted component to the complete response, in effect adding sidelobes to the synthesized beam. From Parseval's theorem, the rms amplitude of the hole-induced sidelobes is proportional to the rms value of the missing spatial sensitivity represented by the holes. Other sidelobes also occur as a result of the oscillations in the $J_1(\pi a_\lambda \theta)/\pi a_\lambda \theta$ profile of the complete response, but there is clearly a sidelobe component from the holes.

5.5 Linear Tracking Arrays

We now consider interferometers or arrays in which the locations of the antennas are confined to a straight line. We have seen that for pairs of antennas with east–west spacings, the tracking loci in the (u, v) plane are a series of ellipses centered on the (u, v) origin. To obtain complete ellipses, it is necessary that the tracking covers a range of 12 h in hour angle. If the antenna spacings of an east–west array increase in uniform increments, the spatial sensitivity is represented by a series of concentric ellipses with uniform increments in their axes. The angular resolution obtained is inversely proportional to the width of the (u, v) coverage in the corresponding
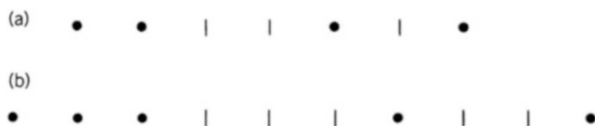
Fig. 5.10 Two linear array configurations in which the antennas are represented by filled circles. (**a**) Arsac's (1955) configuration containing all spacings up to six times the unit spacing, with no redundancy. (**b**) Bracewell's (1966) configuration containing all spacings up to nine times the unit spacing, with the unit spacing occurring twice.

direction; the width in the v direction is equal to that in the u direction times the sine of the declination, δ. East–west linear arrays containing spacings at multiples of a basic interval have found wide use, especially in earlier radio astronomy, for observations at $|\delta|$ greater than $\sim 30°$.

In the simplest type of linear array, the antennas are spaced at uniform intervals ℓ_λ (see Fig. 1.13a). This type of array is sometimes known as a grating array, by analogy with an optical diffraction grating. If there are n_a antennas, such an array output contains $(n_a - 1)$ combinations with the unit spacing, $(n_a - 2)$ with twice the unit spacing, and so on. Thus, short spacings are highly redundant, and one is led to seek other ways to configure the antennas to provide larger numbers of different spacings for a given n_a. Note, however, that redundant observations can be used as an aid in calibration of the instrumental response and atmospheric effects, so some degree of redundancy is arguably beneficial (Hamaker et al. 1977).

Early examples of antenna configurations include one in Fig. 5.10a, used by Arsac (1955), with no redundant spacings. The six possible pair combinations all have different spacings. With more than four antennas, there is always either some redundancy or some missing spacings. A five-element, *minimum-redundancy*[1] configuration devised by Bracewell (1966) is shown in Fig. 5.10b. Moffet (1968) listed examples of minimum-redundancy arrays of up to 11 elements, and solutions for larger arrays are discussed by Ishiguro (1980). Moffet defined two classes. These are restricted arrays in which all spacings up to the maximum spacing, $n_{max}\ell_\lambda$ (that is, the total length of the array), are present; general arrays in which all spacings up to some particular value are present; and also some longer ones. Examples for eight elements are shown in Fig. 5.11. A measure of redundancy for a linear array is given by the expression

$$\frac{1}{2}n_a(n_a - 1)/n_{max} \,, \tag{5.18}$$

which is the number of antenna pairs divided by the number of unit spacings in the longest spacing. This is equal to 1.0 and 1.11 for the configurations in Fig. 5.10a

---

[1]The mathematical theory of minimum redundancy is known as the optimal Golomb ruler (Golomb 1972), which has roots in the mathematical literature going back to the 1930s.
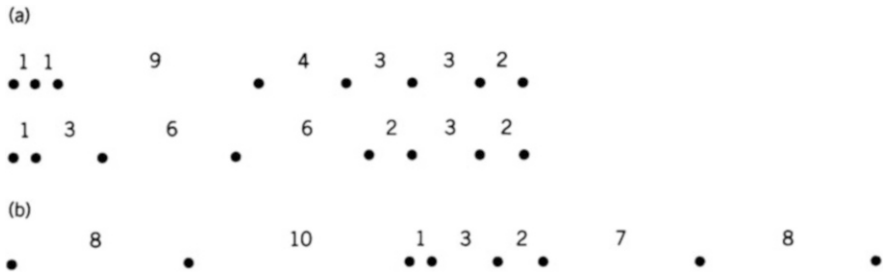
Fig. 5.11 Eight-element, minimum-redundancy, linear arrays: the numbers indicate spacings in multiples of the unit spacing. (**a**) Two arrays that uniformly cover the range of 1 to 23 times the unit spacing. (**b**) An array that uniformly covers 1 to 24 times the unit spacing but has a length of 39 times the unit spacing. The extra spacings are 8, 31 (twice), and 39 times the unit spacing. © 1968 IEEE. Reprinted with permission, from A. T. Moffet (1968).

and 5.10b, respectively. A study in number theory by Leech (1956) indicates that for large numbers of elements, this redundancy factor approaches 4/3. A linear minimum-redundancy array that uses the configuration in Fig. 5.10b is described by Bracewell et al. (1973). For arrays with such small numbers of antennas, the choice of the configuration is particularly important.

The ability to move a small number of elements adds greatly to the range of performance of an array. Figure 5.12 shows the arrangement of three antennas in an early synthesis instrument, the Cambridge One-Mile Radio Telescope (Ryle 1962). Antennas 1 and 2 are fixed, and their outputs are correlated with that from antenna 3, which can be moved on a rail track. In each position of antenna 3, the source under observation is tracked for 12 h, and visibility data are obtained over two elliptical loci in the (u, v) plane. The observation is repeated as antenna 3 is moved progressively along the track, and the increments in the position of this antenna determine the spacing of the elliptical loci in the (u, v) plane. From the sampling theorem (Sect. 5.2.1), the required (u, v) spacing is the reciprocal of the angular width (in radians) of the source under investigation. The ability to vary the incremental spacing adds versatility to the array and reduces the number of antennas required. The configuration of a larger instrument of this type, the Westerbork Synthesis Radio Telescope (Baars and Hooghoudt 1974; Högbom and Brouw 1974; Raimond and Genee 1996), is shown in Fig. 5.13. Here, ten fixed antennas are
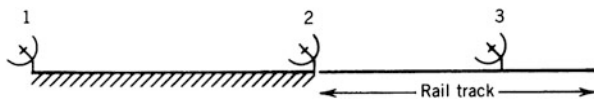

Fig. 5.12 The Cambridge One-Mile Radio Telescope. Antennas 1 and 2 are at fixed locations, and the signals they receive are each correlated with the signal from antenna 3, which can be located at various positions along a rail track. The fixed antennas are 762 m apart, and the rail track is a further 762 m long. The unit spacing is equal to the increment of the position of antenna 3, and all multiples up to 1524 m can be obtained.
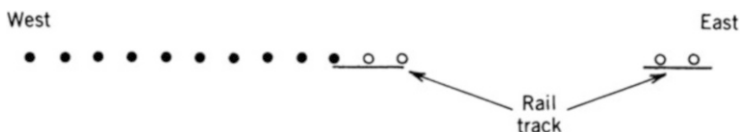
Fig. 5.13 Antenna configuration of the Westerbork Synthesis Radio Telescope. The ten filled circles represent antennas at fixed locations, and the four open circles represent antennas that are movable on rail tracks. The signals from each of the fixed antennas are combined with the signals from each of the movable ones. The diameter of the antennas is 25 m, and the spacing of the fixed antennas is 144 m.

combined with four movable ones, and the rate of gathering data is approximately 20 times greater than with the three-element array.

The sampling of the visibility function at points on concentric, equally spaced ellipses results in the introduction of ringlobe responses. These may be understood by noting that for a linear array, the instantaneous spacings are represented in one dimension by a series of δ functions, as shown in Fig. 5.14a. If the array contains all multiples of the unit spacings up to $N\ell_\lambda$, and if the corresponding visibility measurements are combined with equal weights, the instantaneous response is a series of fan beams, each with a profile of sinc-function form, as in Fig. 5.14b. This follows from the Fourier transform relationship for a truncated series of delta functions (see Appendix 2.1):

$$\sum_{i=-N}^{N} \delta(u - i\ell_\lambda) \longleftrightarrow \frac{\sin\left[(2N+1)\pi\ell_\lambda l\right]}{\pi\ell_\lambda l} * \sum_{k=-\infty}^{\infty} \delta\left(l - \frac{k}{\ell_\lambda}\right) . \tag{5.19}$$

The delta functions on the left side represent the spacings in the u domain. The series on the left is truncated and can be envisaged as selected from an infinite series by multiplication with a rectangular window function. The right side represents the
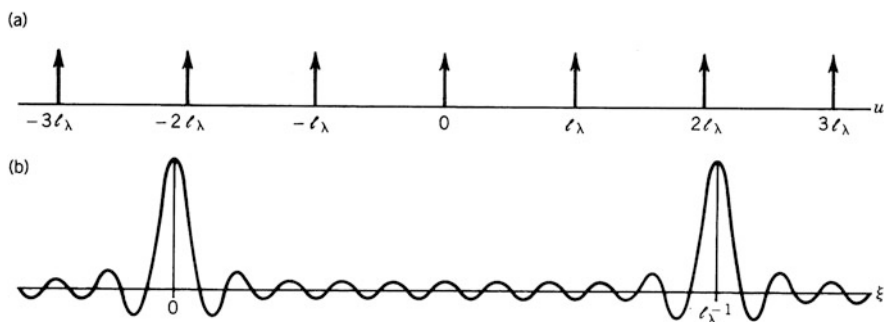

Fig. 5.14 Part of a series of δ functions representing the instantaneous distribution of spacings for a uniformly spaced linear array with equal weight for each spacing. (**b**) Part of the corresponding series of fan beams that constitute the instantaneous response. Parts (**a**) and (**b**) represent the left and right sides of Eq. (5.19), respectively.
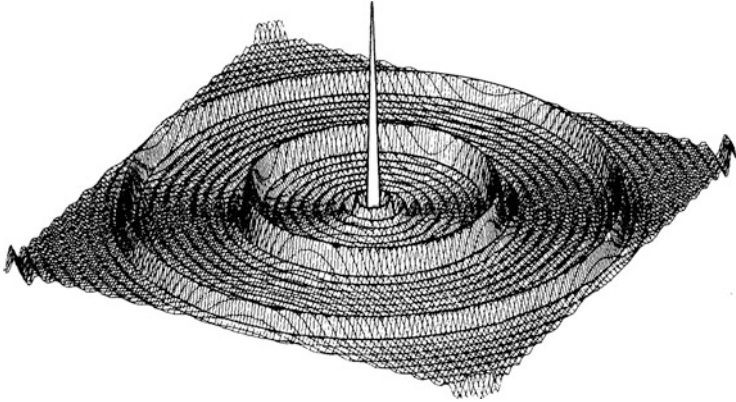
Fig. 5.15 Example of ringlobes. The response of an array for which the spatial transfer function is a series of nine circles concentric with the (u, v) origin, resulting, for example, from observations with an east–west linear array with 12-h tracking at a high declination. The radii of these circles are consecutive integral multiples of the unit antenna spacing. The weighting corresponds to the principal response discussed in Sect. 10.2. From Bracewell and Thompson (1973). © AAS. Reproduced with permission.

beam pattern in which the Fourier transform of the window function is replicated by convolution with delta functions. As the Earth's rotation causes the spacing vectors to sweep out ellipses in the (u, v) plane, the corresponding rotation of the array relative to the sky can be visualized as causing a central fan beam to rotate into a narrow pencil beam, while its neighbors give rise to lower-level, ring-shaped responses concentric with the central beam, as shown in Fig. 5.15. This general argument gives the correct spacing of the ringlobes, the profile of which is modified from the sinc-function form.

If the spatial sensitivity in the (u, v) plane is a series of circular delta functions of radius $q, 2q, \ldots, Nq$, the profile of the kth ringlobe is of the form

$$\text{sinc}^{1/2}\left[2(N + \frac{1}{2})(qr - k)\right] , \tag{5.20}$$

where $r = \sqrt{l^2 + m^2}$. The function $\text{sinc}^{1/2}(\chi)$ is plotted in Fig. 5.16 and is the half-order derivative of $(\sin \pi\chi)/\pi\chi$. It can be computed using Fresnel integrals (Bracewell and Thompson 1973).

The application of the sampling theorem (Sect. 5.2.1) to the choice of incremental spacing requires that the increment be no greater than the reciprocal of the source width. In terms of ringlobes, this condition ensures that the minimum ringlobe spacing is no less than the source width. Thus, if the sampling theorem is followed, the main-beam response to a source just avoids being overlapped by a ringlobe response to the same source. In arrays such as those in Figs. 5.12 and 5.13, ringlobes can be effectively suppressed if the movable antennas are positioned in steps slightly
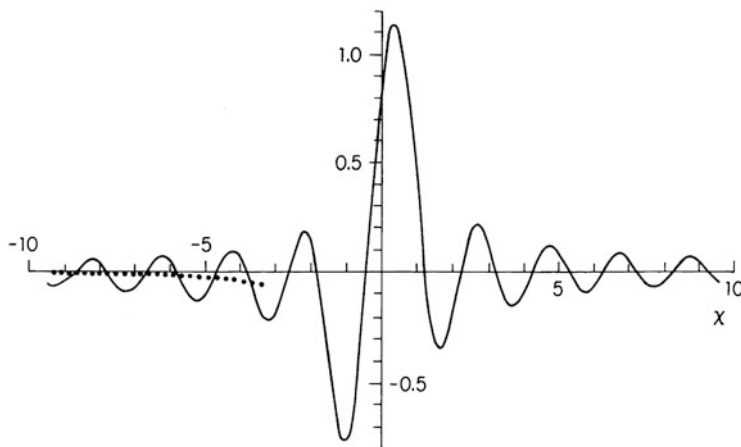
Fig. 5.16 Cross section of a ringlobe in the principal response to a point source of an east–west array with uniform increments in antenna spacing. The left side is the inside of the ring, and the right is the outside. The dotted line indicates a negative mean level of the oscillations on the inner side. From Bracewell and Thompson (1973). © AAS. Reproduced with permission.

less than the antenna diameter, in which case the ringlobe lies outside the primary antenna beam. Note, however, that the first spacing cannot be less than the antenna diameter, and the missing low-spacing measurements may have to be obtained by other means (see the discussion of mosaicking in Sect. 11.5). Ringlobes can also be greatly reduced by image-processing techniques such as the CLEAN algorithm, which is described in Sect. 11.1.

Although the elliptical loci in the (u, v) plane are spaced at equal intervals, the natural weighting of the data for an east–west linear array is not uniform, because in any interval of time, the antenna-spacing vectors move a distance proportional to their length. In the projection of the (u, v) plane onto the equatorial plane of the Earth, which is discussed in Sect. 4.2 as the (u', v') plane, the spacing vectors rotate at constant angular velocity, and the density of measured points is proportional to

$$q'^{-1} = (u'^2 + v'^2)^{-1/2} = (u^2 + v^2 \text{cosec}^2 \delta)^{-1/2} \, . \tag{5.21}$$

In the (u, v) plane, the density of measurements, averaged over an area of dimensions comparable to the unit spacing of the antennas, is inversely proportional to $\sqrt{u^2 + v^2 \text{cosec}^2 \delta}$. Along a straight line through the (u, v) origin, the density is inversely proportional to $\sqrt{u^2 + v^2}$.

5.6   Two-Dimensional Tracking Arrays

As noted previously, the spatial frequency coverage for an east–west linear array becomes severely foreshortened in the v dimension for observations near the celestial equator. For such observations, a configuration of antennas is required in which the Z component of the antenna spacing, as defined in Sect. 4.1, is comparable to the X and Y components. This is achieved by including spacings with azimuths other than east–west. The configuration is then two-dimensional. An array located at an intermediate latitude and designed to operate at low declinations can cover the sky from the pole to declinations of about 30° into the opposite celestial hemisphere. This range includes about 70% of the total sky, that is, almost three times as much as that of an east–west array. Since the Z component is not zero, the elliptical (u, v) loci are broken into two parts, as shown in Fig. 4.4. As a result, the pattern of the (u, v) coverage is more complex than is the case for an east–west linear array, and the ringlobes that result from uniform spacing of the loci are replaced by more complex sidelobe structure. In two dimensions, the choice of a minimum-redundancy configuration of antennas is not as simple as for a linear array. A first step is to consider the desired spatial transfer function $W(u, v)$. There is no direct analytical way to go from $W(u, v)$ to the antenna configuration, but iterative methods of finding an optimum, or near-optimum, solution can be used.

First, consider the effect of tracking a source across the sky, and suppose that for a source near the zenith, the *instantaneous* spatial frequency coverage results in approximately uniform sampling within a circle centered on the (u, v) origin. At any time during the period of tracking of the source, the (u, v) coverage is the zenith coverage projected onto the plane of the sky, with some degree of rotation that depends on the hour angle and declination of the source. The projection results in foreshortening of the coverage from a circular to an elliptical area, still centered on the (u, v) origin, and this foreshortening is least at meridian transit. The effect of observing over a range of hour angle can be envisaged as averaging a range of elliptical (u, v) areas that suffer some rotation of the major axis. At the center of the (u, v) plane will be an area that remained within the foreshortened coverage over the whole observation, and if the instantaneous coverage is uniform, then it will remain uniform within this area. Outside the area, the foreshortening will cause the coverage to taper off smoothly. These effects depend on the declination of the source and the range of hour-angle tracking. Practical experience indicates that some tapering of the visibility measurements is seldom a serious problem. Thus, it can generally be expected that two-dimensional arrays in which the number of antennas is large enough to provide good instantaneous (u, v) coverage will also provide good performance when used with hour-angle tracking.

5.6.1   Open-Ended Configurations

For configurations with open-ended arms such as the cross, T, and Y, the spatial frequency coverage is shown in Fig. 5.7. The spatial frequency coverage of the cross and T has fourfold symmetry in both cases; we ignore the effect of the missing small extensions on the top and bottom sides of the square for the T. The spatial frequency coverage of the equiangular Y-shaped array (120° between adjacent arms) has sixfold symmetry. (n-fold symmetry denotes a figure that is unchanged by rotation through $2\pi/n$. For a circle, n becomes infinite, and other figures approach circular symmetry as n increases.) The autocorrelation function of the equiangular Y-shaped array is closer to circular symmetry than that of a cross or T-shaped array. In this respect, a five-armed array, as suggested by Hjellming (1989), would be better still, but more expensive.

As an example of the open-ended configuration, we examine some details of the design of the VLA (Thompson et al. 1980; Napier et al. 1983; Perley et al. 2009). This array is located at latitude 34° N in New Mexico and is able to track objects as far south as $-30°$ for almost 7 h without going below 10° in elevation. Performance specifications called for imaging with full resolution down to at least $-20°$ declination and for obtaining an image in no more than 8 h of observation without moving antennas to new locations. In designing the array, comparison of the performance of various antenna configurations was accomplished by computing the spatial transfer function with tracking over an hour-angle range ± 4 h at various declinations. In judging the merit of any configuration, the basic concern was to minimize sidelobes in the synthesized beam. It was found that the percentage of holes in the (u, v) coverage was a consistent indication of the sidelobe levels of the synthesized beam, and to judge between different configurations, it was not always necessary to calculate the detailed response (National Radio Astronomy Observatory 1967, 1969). For a given number of antennas, the equiangular Y-shaped array was found to be superior to the cross and T-shaped array; see Fig. 5.17.

Inverting the Y has no effect on the beam, but if the antennas have the same radial disposition on each arm, the performance near zero declination is improved by rotating the array so that the nominal north or south arm makes an angle of about 5° with the north–south direction. Without this rotation, the baselines between corresponding antennas on the other two arms are exactly east–west, and for $\delta = 0°$, the spacing loci degenerate to straight lines that are coincident with the u axis and become highly redundant. The total number of antennas, 27, was chosen from a consideration of (u, v) coverage and sidelobe levels and resulted in peak sidelobes at least 16 dB below the main-beam response, except at $\delta = 0°$, where Earth rotation is least effective. The 27 antennas provide 351 pair combinations.

The positions of the antennas along the arms provide another set of variables that can be adjusted to optimize the spatial transfer function. Figure 5.17 shows two approaches to the problem. Configuration (a) was obtained by using a pseudo-dynamic computation technique (Mathur 1969), in which arbitrarily chosen initial conditions were adjusted by computer until a near-optimum (u, v) coverage was
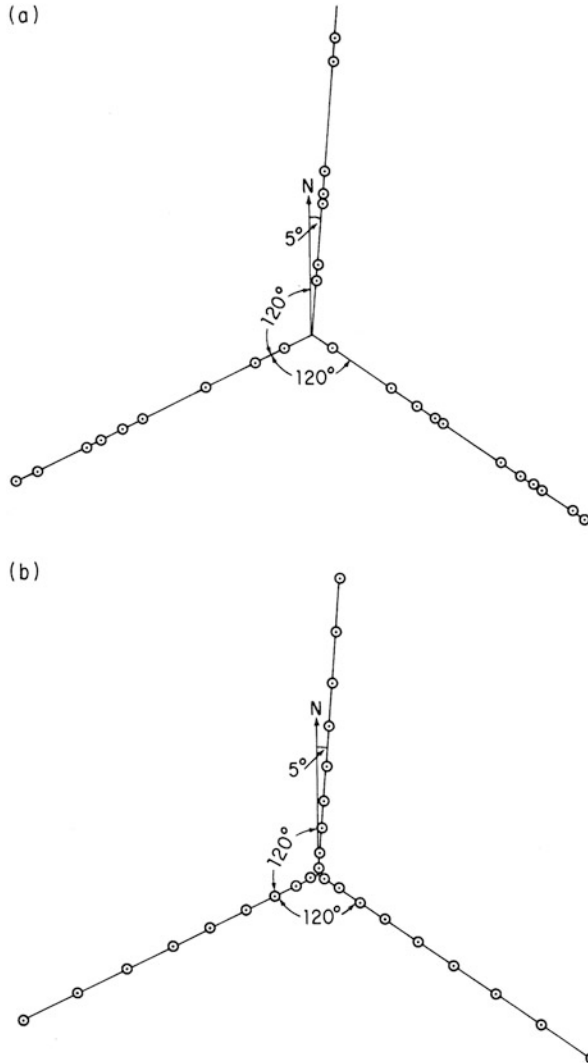
Fig. 5.17 (**a**) Proposed antenna configuration for the VLA that resulted from Mathur's (1969) computer-optimized design. (**b**) Power-law design (Chow 1972) adopted for the VLA. © 1983 IEEE. Reprinted, with permission, from P. J. Napier et al. (1983).

reached. Configuration (b) shows a power-law configuration derived by Chow (1972). This analysis led to the conclusion that a spacing in which the distance of the nth antenna on an arm is proportional to n^α would provide good (u, v) coverage. Comparison of the empirically optimized configuration with the power-law spacing with $\alpha \simeq 1.7$ showed the two to be essentially equal in performance. The power-law result was chosen largely for reasons of economy. A requirement of the design

was that four sets of antenna stations be provided to vary the scale of the spacings in four steps, to allow a choice of resolution and field of view for different astronomical objects. By making α equal to the logarithm to the base 2 of the scale factor between configurations, the location of the nth station for one configuration coincides with that of the $2n$th station for the next-smaller configuration. The total number of antenna stations required was thereby reduced from 108 to 72. Plots of the spatial frequency coverage are shown in Fig. 5.18. The snapshot in Fig. 5.18d shows the instantaneous coverage, which is satisfactory for imaging simple structure in strong sources.
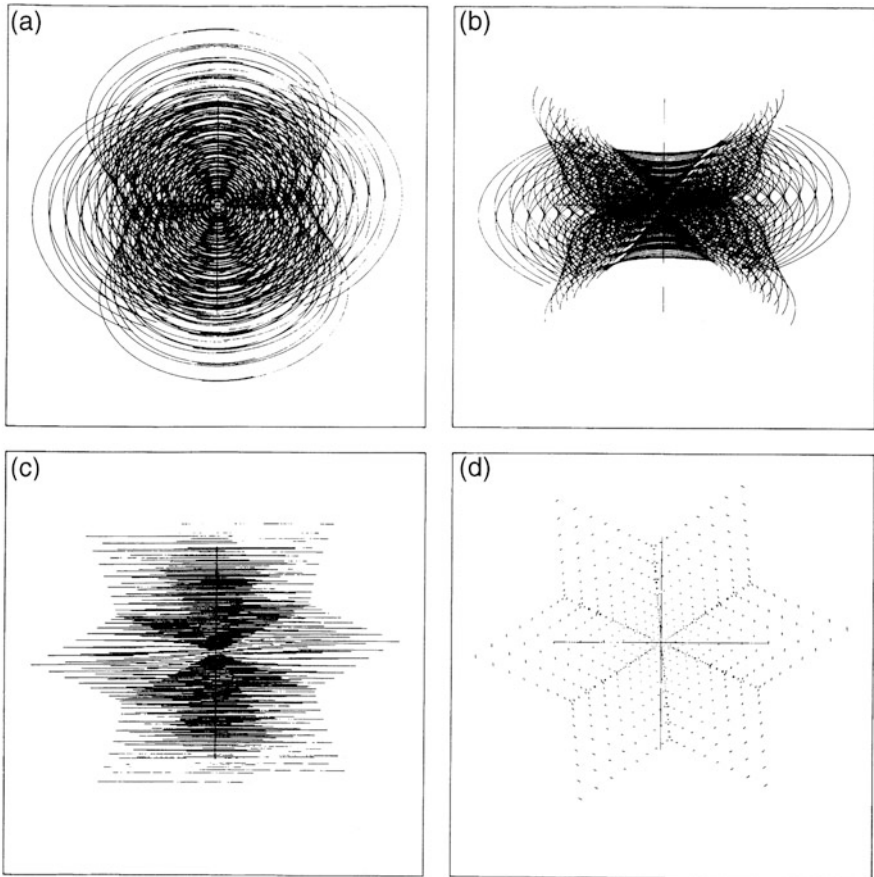

Fig. 5.18 Spatial frequency coverage for the VLA with the power-law configuration of Fig. 5.17b: (**a**) $\delta = 45°$; (**b**) $\delta = 30°$; (**c**) $\delta = 0°$; (**d**) snapshot at zenith. The range of hour angle is ± 4 h or as limited by a minimum pointing elevation of $9°$, and ± 5 min for the snapshot. The lengths of the (u, v) axes from the origin represent the maximum distance of an antenna from the array center, that is, 21 km for the largest configuration. © 1983 IEEE. Reprinted, with permission, from P. J. Napier et al. (1983).

5.6.2   Closed Configurations

The discussion here largely follows that of Keto (1997). Returning to the proposed criterion of uniform distribution of measurements within a circle in the (u, v) plane, we note that a configuration of antennas around a circle (a ring array) provides a useful starting point since the distribution of antenna spacings cuts off sharply in all directions at the circle diameter. This is shown in Fig. 5.7g and h. We begin by considering the instantaneous (u, v) coverage for a source at the zenith. This is shown in Fig. 5.19a for 21 equally spaced antenna locations indicated by triangles. There are 21 antenna pairs at the unit spacing, uniformly distributed in azimuth, and each of these is represented by two points in the (u, v) plane. The same statement can be made for any other paired spacings around the circle. As a result, the spatial transfer function consists of points that lie on a pattern of circles and radial lines. Note also that as the spacings approach the full diameter of the circle, the distance between antennas increases only very slowly. For example, the direct distance between antennas spaced 10 intervals around the circle is very little more than that for antennas at 9 intervals. Thus, there is an increase in the density of measurements at the longest spacings (the points along any radial line become more closely spaced) as well as a marked increase toward the center. Note that the density of points closely follows the radial profile of the autocorrelation function in Fig. 5.7j, except close to the origin, since Fig. 5.19 includes only cross-correlations between antennas.

One way of obtaining a more uniform distribution is to randomize the spacings of the antennas around the circle. The (u, v) points are then no longer constrained to lie on the pattern of circles and lines, and Fig. 5.19b shows an example in which a partial optimization has been obtained by computation using a neural-net algorithm. Keto (1997) discussed various algorithms for optimizing the uniformity of the spatial sensitivity. An earlier investigation of circular arrays by Cornwell (1988) also resulted in good uniformity within a circular (u, v) area. In this case, an optimizing program based on simulated annealing was used, and the spacing of the antennas around the circle shows various degrees of symmetry that result in patterns resembling crystalline structure in the (u, v) spacings.

Optimizing the antenna configurations can also be considered more broadly, and Keto (1997) noted that the cutoff in spacings at the same value for all directions is not unique to the circular configuration. There are other figures, such as the Reuleaux triangle, for which the width is constant in all directions. The Reuleaux triangle is shown in Fig. 5.7i and consists of three equal circular arcs indicated by the solid lines. The total perimeter is equal to that of a circle with diameter equal to one of the sides of the equilateral triangle shown by the broken lines. Similar figures can be constructed for any regular polygon with an odd number of sides, and a circle represents such a figure for which the number tends to infinity. The Reuleaux triangle is the least symmetrical of this family of figures. Other facts about the Reuleaux triangle and similar figures can be found in Rademacher and Toeplitz (1957).
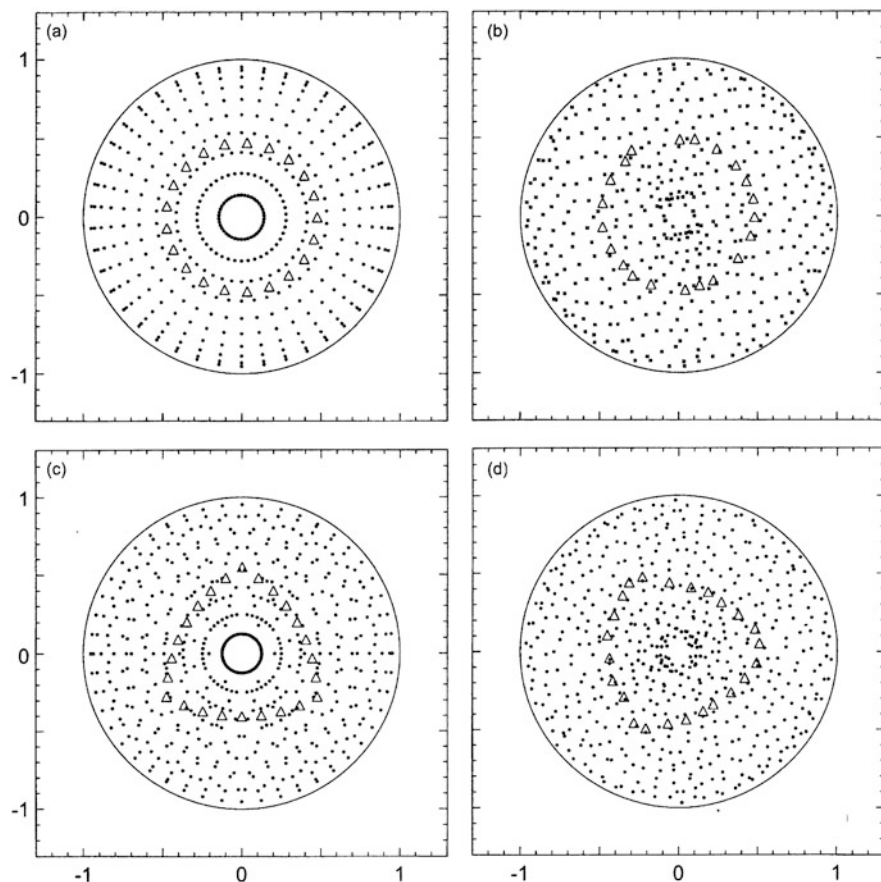
Fig. 5.19 (**a**) A circular array with 21 uniformly spaced antennas indicated by the triangles, and the instantaneous spatial frequency coverage indicated by the points. The scale of the diagrams is the same for both the antenna positions and the spatial frequency coordinates u and v. (**b**) The array and spatial frequency coverage as in (**a**) but after adjustment of the antenna positions around the circle to improve the uniformity of the coverage. (**c**) An array of 24 antennas equally spaced around a Reuleaux triangle, and the corresponding spatial frequency coverage. (**d**) The array and spatial sensitivity as in (**c**) with adjustment of the antenna spacing to optimize the uniformity of the coverage. From Keto (1997). © AAS. Reproduced with permission.

Since the optimization of the circular array in Fig. 5.19b results in a reduction in the symmetry, it may be expected that an array based on the Reuleaux triangle would provide better uniformity in the spatial frequency coverage than the circular array. This is indeed the case, as can be seen by comparing Figs. 5.19a and c, where the spacing between adjacent antennas for both is uniform. The circular array with irregular antenna spacings in Fig. 5.19b was obtained by starting with a circular array and allowing antenna positions to be moved small distances. In this case, the program was not allowed to reach a fully optimized solution. Allowing the

optimization to run to convergence results in antennas at irregular spacings around a Reuleaux triangle, as shown in Fig. 5.19d. This result does not depend on the starting configuration. Comparison of Figs. 5.19b and d shows that the difference between the circle and the Reuleaux triangle is much less marked when they have both been subjected to some randomization of the antenna positions around the figure, although a careful comparison shows the uniformity in Fig. 5.19d to be a little better than in b.

Figure 5.20 shows the spatial frequency coverage for an array in an optimized Reuleaux triangle configuration. The tracking range is ∼ ±3 h of hour angle, and the latitude is equal to that of the VLA. Comparison of these figures with corresponding ones for the VLA in Fig. 5.18 shows that the Reuleaux triangle produces spatial frequency coverage that is closer to the uniformly sampled circular area than does the equiangular Y configuration. As indicated in Fig. 5.7, the autocorrelation function of a figure with linear arms contains high values in directions where the
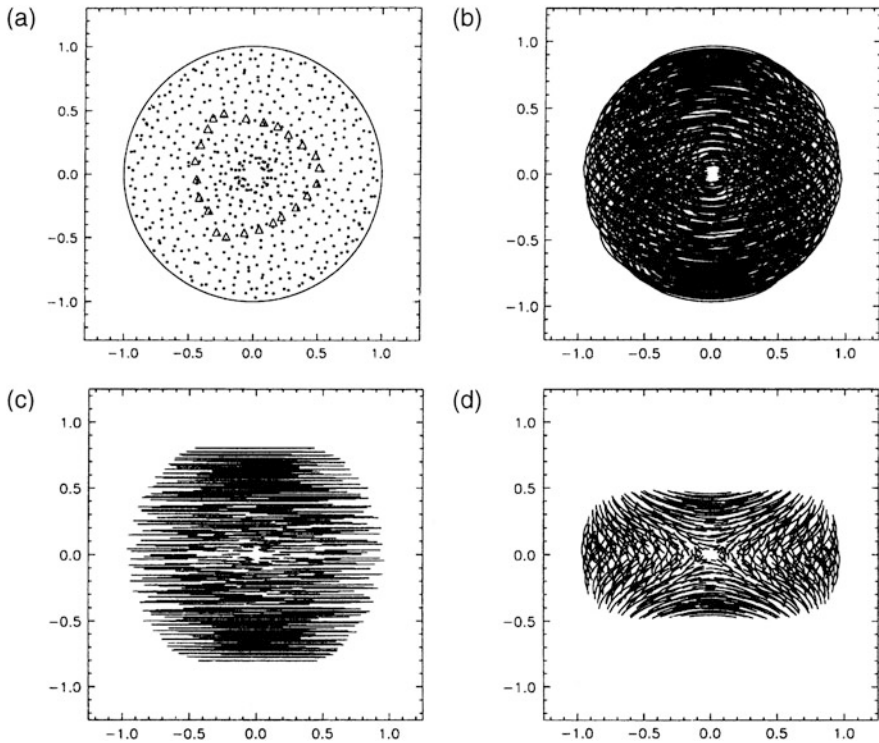

Fig. 5.20 Spatial frequency coverage for a closed configuration of 24 antennas optimized for uniformity of measurements in the snapshot mode: (**a**) snapshot at zenith; (**b**) $\delta = +30°$; (**c**) $\delta = 0°$; (**b**) $\delta = -28°$. The triangles in (**a**) indicate the positions of the antennas. The tracking is calculated for an array at $34°$ latitude to simplify comparison with the VLA (Fig. 5.18). For each declination shown, the tracking range is the range of hour angle for which the source elevation is greater than $25°$. From Keto (1997). © AAS. Reproduced with permission.

arms of overlapping figures line up. This effect contributes to the lack of uniformity in the spatial sensitivity of the Y-shaped array. Curvature of the arms or quasi-random lateral deviations of the antennas from the arms helps to smear the sharp structure in the spatial transfer function. The high values along radial lines do not occur in the autocorrelation function of a circle or similar closed figure, which is one reason why configurations of this type provide more uniform spatial frequency coverage.

Despite some less-than-ideal features of the equiangular Y-shaped array, the VLA produces astronomical images of very high quality. Thus, although the circularity and uniformity of the spatial frequency coverage are useful criteria, they are not highly critical factors. As long as the measurements cover the range of u and v for which the visibility is high enough to be measurable, and the source is strong enough that any loss in sensitivity resulting from nonuniform weighting can be tolerated, excellent results can be obtained. The Y-shaped array has a number of practical advantages over a closed configuration. When several scaled configurations are required to allow for a range of angular resolution, the alternative locations lie along the same arms, whereas with the circle or Reuleaux triangle, separate scaled configurations are required. The flexibility of the Y-shaped array is particularly useful in VLA observations at southern declinations for which the projected spacings are seriously foreshortened in the north–south direction. For such cases, it is possible to move the antennas on the north arm onto the positions for the next-larger configuration and thereby substantially compensate for the foreshortening.

Some further interesting examples of configurations are given below.

- The compact array of the Australia Telescope is an east–west linear array of six antennas, all movable on a rail track (Frater et al. 1992).
- The UTR-2 is a T-shaped array of large-diameter, broadband dipoles built by the Ukrainian Academy of Sciences near Grakovo, Ukraine (Braude et al. 1978). The frequency range of operation is 10–25 MHz. Several smaller antennas of similar type have been constructed at distances up to approximately 900 km from the Grakovo site and are used for VLBI observations.
- An array of 720 conical spiral antennas in a T-shaped configuration operating in the frequency range 15–125 MHz was constructed at Borrego Springs, California (Erickson et al. 1982).
- The Mauritius Radio Telescope, near Bras d'eau, Mauritius, is a T-shaped array of helix antennas operating at 150 MHz. The east–west arm is 2 km long. The south arm is 880 m long and is synthesized by moving a group of antennas on trolleys. The array is similar in principle to the one in Fig. 1.12a. It is intended to cover a large portion of the Southern Hemisphere.
- The GMRT (Giant Metrewave Radio Telescope) near Pune, India, consists of 30 antennas, 16 of which are in a Y-shaped array with curved arms approximately 15 km long. The remaining 14 are in a quasi-random cluster in the central 2 km (Swarup et al. 1991). The antennas are 45 m in diameter and are at fixed locations. The highest operating frequency is approximately 1.6 GHz.

- A circular array with 96 uniformly spaced antennas was constructed at Culgoora, Australia, for observations of the Sun (Wild 1967). This was a multibeam, scanning, phased array rather than a correlator array, consisting of 96 antennas uniformly spaced around a circle of diameter 3 km and operating at 80 and 160 MHz. To suppress unwanted sidelobes of the beam, Wild (1965) devised an ingenious phase-switching scheme called J^2 synthesis. The spatial sensitivity of this ring array was analyzed by Swenson and Mathur (1967).
- The Multielement Radio-Linked Interferometer Network (MERLIN) of the Jodrell Bank Observatory, England, consists of six antennas with baselines up to 233 km (Thomasson 1986).
- The Submillimeter Array (SMA) of the Smithsonian Astrophysical Observatory and Academia Sinica of Taiwan, located on Mauna Kea, Hawaii, is the first array to be built using a Reuleaux triangle configuration (Ho et al. 2004).
- In large arrays in which the antennas cover areas extending over several kilometers, there is usually a central area with relatively dense antenna coverage, surrounded by extensive areas with sparser coverage. These outer parts may be in the form of extended arms, but the placement of the individual antennas is often irregular as a result of details of the landscape. Examples include ALMA (Wootten and Thompson 2009), the Murchison Widefield Array (Lonsdale et al. 2009), the Australian SKA Pathfinder (DeBoer et al. 2009), and the Low-Frequency Array (LOFAR) (de Vos et al. 2009). For discussion of projects for large arrays, see Carilli and Rawlings (2004).

5.6.3 VLBI Configurations

In VLBI (very-long-baseline interferometry) arrays, which are discussed in more detail in Chap. 9, the layout of antennas results from considerations of both (u, v) coverage and practical operating requirements. During the early years of VLBI, the signals were recorded on magnetic tapes that were then sent to the correlator location for playback. The use of tape has been superseded by magnetic disks and in some cases by direct transmission of the signals to the correlator using fiberoptic or other transmission media. Observing periods are limited by the ranges of hour angle and declination that are simultaneously observable from widely spaced locations. Although these locations usually deviate significantly from a plane, the angular widths of the sources under observation are generally sufficiently small that the small-field approximation (i.e., l and m small) can be used in deriving the radio image, as in Eq. (3.9).

For the first two decades after the inception of the VLBI technique, observations were mainly joint ventures among different observatories. Consideration of arrays dedicated solely to VLBI occurred as early as 1975 (Swenson and Kellermann 1975), but construction of such arrays did not begin for another decade. A study of antenna locations for a VLBI array has been discussed by Seielstad et al. (1979).

To obtain a single index as a measure of the performance of any configuration, the spatial transfer function was computed for a number of declinations. The fraction of appropriately sized (u, v) cells containing measurements was then weighted in proportion to the area of sky at each declination and averaged. Maximizing the index, in effect, minimizes the number of holes (unfilled cells). Other studies have involved computing the response to a model source, synthesizing an image, and improving the model as necessary.

The design of an array dedicated to VLBI, the Very Long Baseline Array (VLBA) of the United States, is described by Napier et al. (1994). The antenna locations [and associated (u, v) loci] are shown in Fig. 5.21 and listed in Table 5.1. A discussion of the choice of sites is given by Walker (1984). Antennas in Hawaii and St. Croix provide long east–west baselines. New Hampshire to St. Croix is the longest north–south spacing. A site in Alaska would be farther north but would be of limited benefit because it would provide only restricted accessibility for sources at southern declinations. An additional site within the Southern Hemisphere would enhance the (u, v) coverage at southern declinations. The southeastern region of the United States is avoided because of the higher levels of water vapor in the atmosphere. Intermediate north–south baselines are provided by the drier West Coast area. The Iowa site fills in a gap between New Hampshire and the southwestern sites. The short spacings are centered on the VLA, and as a result, the spatial frequency coverage shows a degree of central concentration. This enables the array to make measurements on a wider range of source sizes than would be possible with the same number of antennas and more uniform coverage. However, this results in some sacrifice in capability for imaging complex sources.

5.6.4 Orbiting VLBI Antennas

The discussion of placing a VLBI station in Earth orbit to work with ground-based arrays started as early as 1969 (Preston et al. 1983; Burke 1984; Kardashev et al. 2013). The combination of orbiting VLBI (OVLBI) and ground-based antennas has several obvious advantages. Higher angular resolution can be achieved, and the ultimate limit may be set by interstellar scintillation (see Sect. 14.4). The orbital motion of the spacecraft helps to fill in the coverage in the (u, v) plane and has the potential to improve the detail and dynamic range in the resulting images. Furthermore, a satellite in low Earth orbit provides rapid (u, v) plane variation, which can be valuable for obtaining information on time variability of source structure.

Figure 5.22 shows an example of the (u, v) coverage for observations with the VSOP project spacecraft known as HALCA (Hirabayashi et al. 1998) and a series of terrestrial antennas: one at Usuda, Japan, one at the VLA site, and the ten VLBA antennas. The spacecraft orbit is inclined at an angle of 31° to the Earth's equator, and the height above the Earth's surface is 21,400 km at apogee and 560 km at perigee. The mission of this spacecraft was to extend the resolution by a factor of
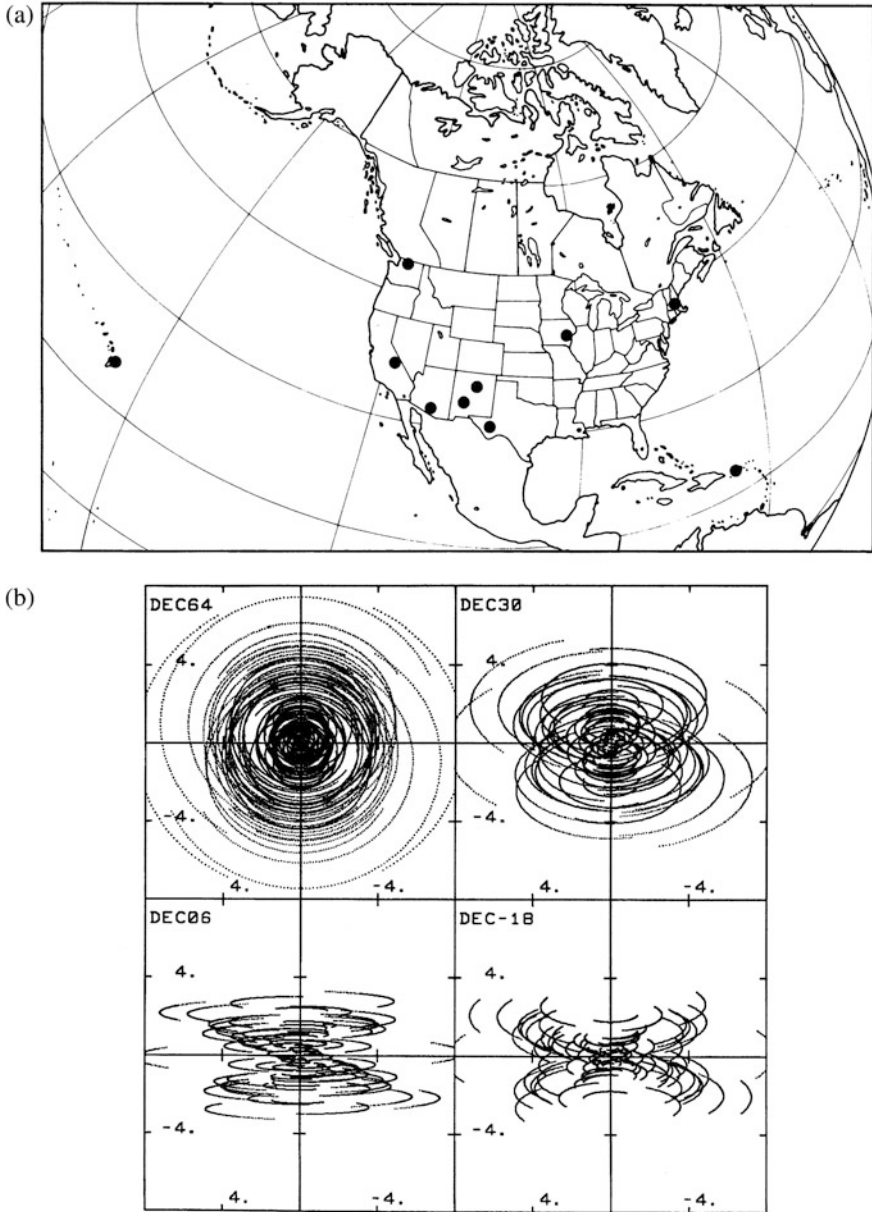
Fig. 5.21 Very Long Baseline Array in the United States: (**a**) locations of the ten antennas, and (**b**) spatial frequency coverage (spacings in thousands of kilometers) for declinations of 64°, 30°, 6°, and −18°, in which the observing time at each antenna is determined by an elevation limit of 10°. From Walker (1984). Reprinted with the permission of and © Cambridge University Press.

Table 5.1 Locations of antennas in the VLBA[a]

Location	N. Latitude (deg min sec)	W. Longitude (deg min sec)	Elevation (m)
St. Croix, VI	17 45 30.57	64 35 02.61	16
Hancock, NH	42 56 00.96	71 59 11.69	309
N. Liberty, IA	41 46 17.03	91 34 26.35	241
Fort Davis, TX	30 38 05.63	103 56 39.13	1615
Los Alamos, NM	35 46 30.33	106 14 42.01	1967
Pie Town, NM	34 18 03.61	108 07 07.24	2371
Kitt Peak, AZ	31 57 22.39	111 36 42.26	1916
Owens Valley, CA	37 13 54.19	118 16 33.98	1207
Brewster, WA	48 07 52.80	119 40 55.34	255
Mauna Kea, HI	19 48 15.85	155 27 28.95	3720

[a]© 1994 IEEE. Reprinted, with permission, from P. J. Napier et al. (1994).
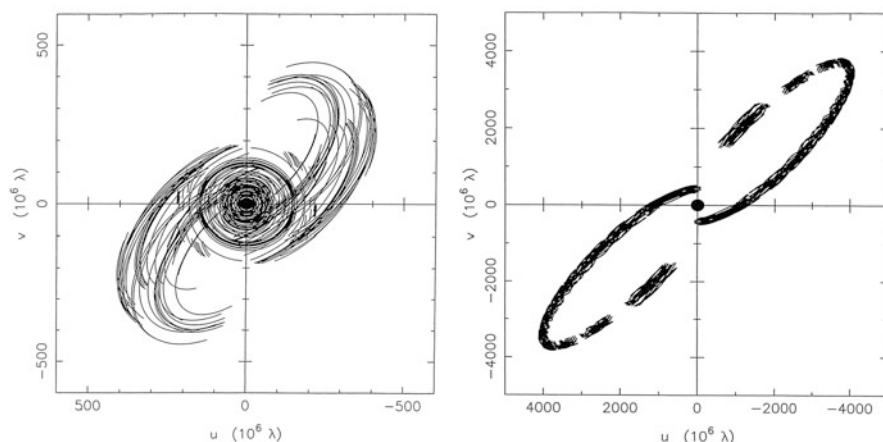

Fig. 5.22 (u, v) plane tracks for arrays with a satellite station for the source 1622+633 at 5 GHz. (**left**) Coverage with VSOP and 12 ground-based antennas. The roughly circular tracks within $2 \times 10^6 \lambda$ are the baselines among the ground-based antennas. Produced with the FAKESAT software developed by D. W. Murphy, D. L. Meier, and T. J. Pearson. (**right**) Coverage with RadioAstron and six ground-based antennas. The gaps in the coverage correspond to actual satellite constraints for hypothetical observations in February 2016. The satellite period is 8.3 days, and the "wobbly" appearance of the tracks is caused by the Earth's diurnal motion. Produced with the FAKERAT software, a derivative of FAKESAT (http://www.asc.rssi.ru/radioastron/software/fakerat).

three over ground-based arrays and to retain good imaging capability. The spacings shown are for a frequency of 5 GHz, and the units of u and v are 10^6 wavelengths; the maximum spacing is 5×10^8 wavelengths, which corresponds to a fringe width of 0.4 mas. The approximately circular loci at the center of the figure represent baselines between terrestrial antennas. The orbital period is 6.3 h, and the data shown correspond to an observation of duration about four orbital periods. The

spacecraft orbit precesses at a rate of order 1° per day, and over the course of one to two years, the coverage of any particular source can be improved by combining observations.

Figure 5.22 also shows examples of the (u, v) coverage for observations with the RadioAstron project spacecraft known as Spektr-R (Kardashev et al. 2013) and a set of ground-based antennas. The spacecraft orbit is inclined at an angle of 80° to the Earth's equator, and, for the case shown here, the ellipticity is 0.86, and the height above the Earth's surface is 289,000 km at apogee and 47,000 km at perigee (orbit on April 14, 2012). The mission of RadioAstron is to provide ultrahigh resolution to explore new astrophysical phenomena while sacrificing imaging quality because of the gap between satellite–Earth and Earth-only baselines. The orbital period is 8.3 days. The orbit evolves substantially with time because of the influences of the Sun and Moon. Occasions when the orbit eccentricity reaches its maximum of 0.95 offer opportunities for better imaging capability.

Figure 5.23 shows an example of the (u, v) coverage that could be obtained between two spacecraft in circular orbits of radius about ten Earth radii, with orthogonal planes that have periods differing by 10%. Multispacecraft operation offers satellite-to-satellite baselines, which are free from the effects of atmospheric delay. In practice, there are likely to be restrictions on coverage resulting from the limited steerability of the astronomy and communication antennas relative to the spacecraft. It is necessary for the spacecraft to maintain an attitude in which the solar power panels remain illuminated and the communications antenna can be pointed toward the Earth. Further discussion of orbiting VLBI is given in Sect. 9.10.
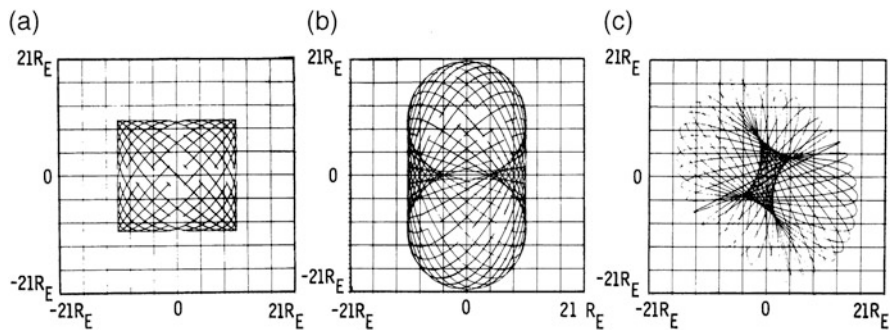

Fig. 5.23 Spatial frequency coverage for two antennas on satellites with circular orbits of radius approximately ten times the Earth's radius R_E: (**a**) source along the X axis; (**b**) source along Y or Z axes; (**c**) source centered between X, Y, and Z axes. The orbits lie in the XY and XZ planes of a rectangular coordinate system. The satellite periods differ by 10%, and the observing period is approximately 20 days. From R. A. Preston et al. (1983), © Cépaduès Éditions, 1983.

5.6.5 Planar Arrays

Studies of cosmic background radiation and the Sunyaev–Zel'dovich effect require observations with very high brightness sensitivity at wavelengths of order 1 cm and shorter: see also Sect. 10.7. Unlike the sensitivity to point sources, the sensitivity to a broad feature that largely fills the antenna beam does not increase with increasing collecting area of the antenna. Thus, for cosmic background measurements, large antennas are not required. Extremely good stability is necessary to allow significant measurements at the level of a few tens of microkelvins per beam, that is, of order $10~\mu Jy~arcmin^{-2}$. Special arrays have been designed for this purpose. A number of antennas are mounted on a platform, with their apertures in a common plane. The whole structure is then supported on an altazimuth mount so the antennas can be pointed to track any position on the sky. An example of such an instrument, the Cosmic Background Imager (CBI), was developed by Readhead and colleagues at Caltech (Padin et al. 2001). Thirteen Cassegrain focus paraboloids, each of diameter 90 cm, were operated in the 26- to 36-GHz range. In this instrument, the antenna mounting frame had the shape of an irregular hexagon with threefold symmetry and maximum dimensions of approximately 6.5 m, as shown in Fig. 5.24. For the particular type of measurements required, the planar array has a number of desirable properties compared with a single antenna of similar aperture, or a number of individually mounted antennas, as outlined below:

- The use of a number of individual antennas allows the output to be measured in the form of cross-correlations between antenna pairs. Thus, the output is not sensitive to the total power of the receiver noise but only to correlated signals entering the antennas. The effects of gain variations are much less severe than
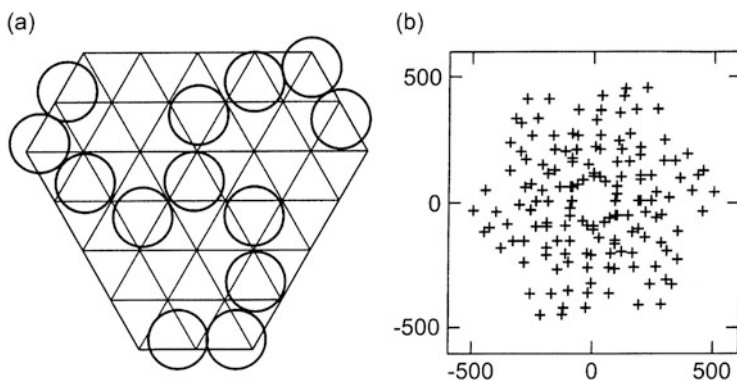

Fig. 5.24 (**a**) Face view of the antenna platform of the Cosmic Background Imager, showing a configuration of the 13 antennas. (**b**) The corresponding antenna spacings in (u, v) coordinates for a wavelength of approximately 1 cm.

in the case of a total-power receiver. Thermal noise from ground pickup in the sidelobes is substantially resolved.

- The antennas can be mounted with the closest spacing physically possible. There are then no serious gaps in the spatial frequencies measured, and structure can be imaged over the width of the primary antenna beams. The apertures cannot block one another because the antenna platform tracks, as can occur for individually mounted antennas in closely spaced arrays.

- In the array in Fig. 5.24, the whole antenna mounting platform can be rotated about an axis normal to the plane of the apertures. Thus, rotation of the baselines can be controlled as desired and is independent of Earth rotation. For a constant pointing direction and rotation angle relative to the sky, the pattern of (u, v) coverage remains constant as the instrument tracks. Variations in the correlator outputs with time can result from ground radiation in the sidelobes, which varies with azimuth and elevation as the array tracks. This variation can help to separate out the unwanted response.

- The close spacing of the antennas results in some cross coupling by which spurious correlated noise is introduced into the receiving channels of adjacent antennas. However, because the antennas are rigidly mounted, the coupling does not vary as the system tracks a point on the sky, as is the case for individually mounted antennas. The effects of the coupling are therefore more easily calibrated out. In the CBI design, the coupling is reduced to -110 to -120 dB by the use of a cylindrical shield around each antenna and by designing the subreflector supports to minimize scattering.

At a frequency of 30 GHz, a pointing error of $1''$ in a 6-m baseline produces a visibility phase error of $1°$. Pointing accuracy is critical, and the CBI antenna is mounted in a retractable dome to shield it from wind, which can be strong at the 5000-m-elevation site at Llano de Chajnantor, Chile. Observations of the cosmic microwave background with this system are briefly described in Sect. 10.7.

5.6.6 Some Conclusions on Antenna Configurations

The most accurate prediction of the performance of an array is obtained by computation of the response of the particular design to models of sources to be observed. However, here we are more concerned with broad comparisons of various configurations to illustrate the general considerations in array design. Some conclusions are summarized below.

- A circle centered on the (u, v) origin can be considered an optimum boundary for the distribution of measurements of visibility. Uniformity of the distribution within the circle is a further useful criterion in many circumstances. An exception is the condition in which sidelobes of the synthesized beam are a serious problem, for example, in low-frequency arrays operating in conditions of source confusion. In arrays in which the scale of the configuration cannot be varied to accommodate

a wide range of source dimensions, a centrally concentrated distribution allows a greater range of angular sizes to be measured with a limited number of antennas. If sensitivity to broad, low-brightness objects is important, it is preferable to have more antenna pairs with short spacings at which such sources are not highly resolved. Note that two of the largest arrays in which the antennas are not movable, the GMRT (in India) and the VLBA (North America), each have a cluster of antennas at relatively short spacings, as well as other antennas at longer spacings, in order to cover a wide range of source dimensions.

- Although the effect of sidelobes on the synthesized beam can be greatly reduced by CLEAN and other image-processing algorithms described in Chap. 11, obtaining the highest dynamic range in radio images (that is, a range of reliable intensity measurements of order 10^6 or more) requires both good spatial frequency coverage and effective image processing. Reducing holes (unsampled cells), which are found to be a consistent indicator of sidelobe levels in this coverage, is a primary objective in array design.
- The east–west linear array has been used for both large and small instruments and requires tracking over ± 6 h to obtain full two-dimensional coverage. It is most useful for regions of the sky within about 60° of the celestial poles and is the most economical configuration with respect to land use for road or rail track.
- The equiangular Y-shaped array gives the best spatial frequency coverage of the existing configurations with linear, open-ended arms. Autocorrelation functions of configurations with odd numbers of arms have higher-order symmetry than those with even numbers in which opposite arms are aligned. Curvature of the arms or random displacement of the antennas helps to smooth out the linear ridges in the (u, v) coverage (e.g., in the snapshot in Fig. 5.18). Such features are also smoothed out by hour-angle tracking and are most serious for snapshot observations.
- The circle and Reuleaux triangle provide the most uniform distributions of measurements. With uniformly spaced antennas, the Reuleaux triangle provides more uniform (u, v) coverage than the circle, but varying the spacing in a quasi-random manner greatly improves both cases and reduces the difference between them; see Fig. 5.19. However, if higher resolution is needed, these configurations are not so easily extended as ones with open-ended arms.

5.7   Implementation of Large Arrays

Of the large arrays that have contributed prominently to progress in radio astronomy, those that developed first have largely been in the range of roughly 500 MHz to 30 GHz, i.e., approximately the wavelength range of 1–60 cm. Examples are the VLA and the arrays at Westerbork (the Netherlands) and the Australia Telescope at Narrabri (Australia). This wavelength range is most conducive for construction of large parabolic reflectors with surface accuracy better than $\sim 1/16$ of a wavelength. Arrays for millimeter-wavelength observations such as the SMA on Mauna Kea

followed a decade or two later, as technology for more accurate surfaces developed, leading to ALMA on the Atacama plateau in Chile, which came into operation in 2013 (Wootten and Thompson 2009). For the 12-m-diameter antennas of ALMA, the specified surface accuracy is less than 25 μm, allowing useful operation up to a frequency of almost 1 THz. For details of measuring and adjusting the surface, see Mangum et al. (2006), Snel et al. (2007), and papers in Baars et al. (2009). The main ALMA array consists of 50 12-m-diameter antennas movable between foundation pads that allow a wide range of spacings up to $\sim$ 15 km. A second, compact, array uses 12 7-m-diameter antennas, and 4 other antennas are available for total power measurements.

At the long-wavelength end of the spectrum, radio astronomy was, for the first few decades, largely limited to measurements of relatively small numbers of the stronger sources, for example, Erickson et al. (1982). A major problem is presented by the ionosphere, calibration of the effects of which requires that the antenna elements be arranged in phased clusters, or subarrays, the beams of which are no wider than the aplanatic structure of the ionosphere. The outputs of these clusters are cross-correlated to provide the visibility values. These long-wavelength observations are important for the study of the most distant Universe including redshifted neutral hydrogen just prior to the Epoch of Reionization. In LOFAR [de Vos et al. (2009) and van Haarlem et al. (2013)], the clusters of dipoles have diameters of $\sim$ 81 m for 10–90 MHz and $\sim$ 40 m for 115–240 MHz. LOFAR is based in the Netherlands, and baselines between the clusters extend up to 1200 km in a generally eastward direction. The dipoles take the form of an inverted V configuration, in which four conductors run outward and downward at an angle of 45° from a point roughly 2 m above the ground, forming two orthogonal dipoles over a ground plane. Note that since the need to calibrate the effect of the ionosphere places a lower limit on the size of the dipole clusters that are used, in this long-wavelength range, large-scale arrays are generally the most successful.

5.7.1 Low-Frequency Range

At frequencies up to about 300 MHz, arrays of broadband dipoles mounted over a ground-plane reflecting screen provide a very practical antenna system. Dipoles are robust, and crossed dipoles provide full polarization coverage. Low-noise transistor front ends can operate at ambient temperature at these frequencies, where the system noise level is set largely by radiation from the sky. Signals from groups of dipoles are combined and the phases adjusted to form beams that can be pointed as required without the need for moving parts. If the spacing between the centers of the dipoles is greater than $\lambda/2$, the array is described as sparse. The collecting area is maximized at $\lambda^2/4$ per element, but because of the spacing, the grating sidelobes begin to be significant as $\lambda/2$ is exceeded. If the spacing is less than $\lambda/2$, the array is described as compact. The effective area is then less than $\lambda^2/4$ per element, but grating lobes are avoided. The variation of the path length through the ionosphere is

a serious problem in imaging at these low frequencies, but it is possible to calibrate the ionosphere over a wide angular range by forming beams in the directions of calibration sources for which the positions are accurately known. LOFAR and the Murchison Widefield Array (Lonsdale et al. 2009) and the Allen Telescope Array (Welch et al. 2009) are examples of this type.

Ellingson (2005) describes a system using dipoles below 100 MHz. To achieve the maximum sensitivity, it is necessary only to match the antennas to the receivers sufficiently well that the total noise is dominated by the background component received by the antennas. This is an advantageous situation since it allows the dipoles to be used over a much wider frequency range than is possible when the impedance must be well matched. To investigate the performance of an inverted-V dipole under these conditions, let γ be the power ratio of the background noise received from the sky to the noise contributed by the receiver. Then we have

$$\gamma \simeq e_r \frac{T_{\text{sky}}}{T_{\text{rec}}} (1 - |\Gamma^2|) \,, \tag{5.22}$$

where e_r (< 1) is an efficiency factor that results largely from the ohmic losses in the ground and in the dipole, T_{sky} is the noise brightness temperature of the sky, T_{rec} is the noise temperature of the receiver, and Γ is the voltage reflection coefficient at the antenna looking toward the receiver. Γ is given by

$$\Gamma = \frac{Z_{\text{rec}} - Z_{\text{ant}}}{Z_{\text{rec}} + Z_{\text{ant}}} \,, \tag{5.23}$$

where Z_{rec} and Z_{ant} are the impedances at the receiver and antenna terminals, respectively. For dominance of the sky noise, one can take γ greater than ~ 10. T_{sky} is related to the intensity of the background radiation I_ν (W m^{-2} Hz^{-1} sr^{-1}), by $T_{\text{sky}} = c^2 I_\nu / 2k\nu^2$, where c is the speed of light and k is Boltzmann's constant. An expression for the sky background intensity I_ν as a function of frequency is given by Dulk et al. (2001) based on measurements by Cane (1979):

$$I_\nu = I_g \nu^{-0.52} \frac{1 - e^{-\tau(\nu)}}{\tau(\nu)} + I_{eg} \nu^{-0.80} e^{-\tau(\nu)} \,, \tag{5.24}$$

where $I_g = 2.48 \times 10^{-20}$ W m^{-2} Hz^{-1} sr^{-1} is the galactic component of the intensity, $I_{eg} = 1.06 \times 10^{-20}$ W m^{-2} Hz^{-1} sr^{-1} is the extragalactic component, and $\tau(\nu) = 5.0\nu^{-2.1}$. This model applies broadly over the sky except near the galactic plane where higher intensities are encountered. In the system described by Ellingson (2005), a wide frequency response for the dipoles is obtained with Z_{rec} in the range 200–800 ohms. Computed responses indicate usable beamwidths in the range 120–140°. Stewart et al. (2004) describe design of an inverted-V dipole in which the effective width of the conducting arms is increased in one dimension, which reduces the impedance variation with frequency compared with that of a dipole with single-wire elements.

5.7.2   *Midfrequency and Higher Ranges*

In the midfrequency range, approximately 0.3–2 GHz, there are two main possibilities. For the frequencies up to about 1 GHz, aperture arrays (van Ardenne et al. 2009) can take the form of half-wave dipoles over a ground screen or, especially at the shorter wavelengths, arrays of Vivaldi antennas (Schaubert and Chio 1999) are used. The Vivaldi elements are formed on strips of aluminum or of copper-clad insulating board. By using two sets of Vivaldi elements running in orthogonal directions, full polarization is obtained. The approximate spacing between adjacent Vivaldi elements is $\lambda/2$, and approximately four amplifiers are required for each square wavelength of collecting area, e.g., $\sim$ 44 amplifiers per square meter at 1 GHz. Aperture arrays provide multiple beams with rapid and flexible pointing.

5.7.2.1   Phased-Array Feeds

For the range from $\sim$ 700 MHz and above, parabolic dish-type antennas with single or multiple beams become more practicable than aperture arrays since, for a given collecting area, they do not require such large numbers of low-noise amplifiers and phasing components. With feeds in the form of a focal-plane array, i.e., an array of individual feed elements in the focal plane of an antenna, it is usually not possible to get the feeds close enough together to avoid gaps between the individual beams. Thus, it is often preferable to use phased-array feeds in which an array of closely spaced receiving elements is arranged in the focal plane. Any one antenna beam is formed as a phased combination of the signals from a number of the feed elements, and such combinations can be designed to provide optimum beam spacings for efficient sky coverage. It is the beamformer that distinguishes the phased-array feed from the focal-plane array. The elements are individually terminated with matched amplifiers, but mutual coupling between the elements cannot be avoided, so the design and adjustment of phased-array feeds is generally more critical than for focal-plane arrays. A general analysis of a phased-array feed can be found in van Ardenne et al. (2009) and Roshi and Fisher (2016).

Designs of phased-array feeds include ones using the Vivaldi system mentioned above and others using a "checkerboard" conductor pattern (Hay et al. 2007). The checkerboard scheme can be envisaged as a series of conducting elements on a circuit board that are arranged like the black squares of a checkerboard. At each point where two corners of conducting squares meet, the corners do not touch, but each feeds one input of a balanced amplifier. The patterns of conducting and nonconducting surfaces are identical and thus self-complimentary. A screen of this form in free space is well matched with load impedances of 377 ohms between the corner pairs of conducting squares where the amplifiers are connected.[2] For use

---

[2]This follows from a formula by Booker: see, e.g., *Antennas*, J. D. Kraus (1950 or later edition).

as a feed array, the checkerboard screen is mounted over a ground plane, which introduces some frequency variation in the impedance. In this frequency range, the input stages of amplifiers at the feeds may be cryogenically cooled to minimize the system temperature.

The use of phased-array feeds in interferometric arrays presents a huge challenge in signal processing because separate correlators are required for each beam. The first interferometer to be designed specifically for phased-array feed technology is ASKAP at the Murchison Radio Observatory. The system has 36 dual-polarized beams operating in the 0.7–1.8 GHz band (Hay et al. 2007; Hotan et al. 2014). A 52-element phased array called APERTIF at 21-cm wavelength has been implemented on the Westerbork telescope (van Cappellen and Bakker 2010; van Cappellen et al. 2011; and Ivashina et al. 2011).

5.7.2.2 Optimum Antenna Size

An array with fixed collecting area can be built with a large number of small antennas (called the "large N, small d solution") or a small number of large antennas (the "small n, large D solution"). Determining the right antenna size is a complex problem. With smaller antennas, the field of view is larger, which enhances survey speed, but with larger antennas, phase calibration sources can be found closer to the target.

A cost analysis is an important element in the determination of antenna size. The critical fact in cost optimization is that the cost of parabolic antenna elements of diameter D scales approximately as $D^{2.7}$ (Meinel 1979). Because the exponent on D is greater than two, the total cost of the antennas in an array increases with diameter for a fixed array area. On the other hand, a larger array of smaller antennas requires more receivers and a larger correlator. A crude cost model can be written

$$C + f_1 n_a D^{2.7} + f_2 n_a + f_3 n_a^2 , \qquad (5.25)$$

where n_a is the number of antennas, f_1 is the antenna cost factor, f_2 is the receiver cost factor, and f_3 is the correlator cost factor, where we assume the correlator cost scales as n_a^2. For a fixed array collecting area, A,

$$n_a = \frac{A}{(\pi \eta D^2 / 4)} , \qquad (5.26)$$

where η is the aperture efficiency. We can substitute Eq. (5.26) into Eq. (5.25) and find the value of D that minimizes C. These values of D are typically in the range of 4 to 20 m. The proposals for the antenna sizes for ALMA ranged in diameter from 6 to 15 m before the decision was made for 12-m-diameter elements, based on cost and many other factors.

5.7.3   Development of Extremely Large Arrays

The concept of an array with a collecting area of $\sim$ 1 square kilometer arose in the late 1990s after the Westerbork Synthesis Radio Telescope, the VLA, and similar instruments had demonstrated the power of the synthesis technique in high-resolution imaging and in cataloging and studying large numbers of sources. Such an array would have a collecting area of about two orders of magnitude greater than existing arrays at that time but would require significant technological development to be financially feasible. An initial objective was to extend the redshift range at which HI in galaxies can be studied by an order of magnitude to $z \sim 2$. The concept has been developed into a plan to build multiple arrays spanning the frequency interval of 70 MHz to greater than 25 GHz, with baselines up to about 5000 km. This instrument, collectively called the Square Kilometre Array (SKA)[3] would have an enormous impact on a broad range of astronomical problems from planet formation to cosmology. The science case for the instrument has been presented by Carilli and Rawlings (2004) and Bourke et al. (2015). Technical details are given in Hall (2004) and Dewdney et al. (2009). The concept of such an array has led to the development of several smaller arrays to test the practicality and performance of possible technologies, including antenna and correlator designs. These include ASKAP, with 12-m-diameter antennas with a checkerboard phased-array feed system providing multiple beams (see Sect. 5.7.2.1), located in Western Australia (DeBoer et al. 2009), and MeerKAT, an array of low-cost 12-m-diameter dish antennas with single-pixel feeds to cover 0.7–10 GHz, located in the Karoo region of South Africa (Jonas 2009).

5.7.4   The Direct Fourier Transform Telescope

The normal practice in radio astronomy is to measure the correlation function of the incident electric field and then take its Fourier transform to obtain the image of the source intensity distribution. An alternative approach is to measure the Fourier transform of the incident electric field with a uniform array of antennas and take its square modulus to obtain the image. Either the correlation function or the direct Fourier transform approach must be implemented at the Nyquist rate appropriate for the bandwidth. The latter approach is simply an implementation of the Fraunhofer diffraction equation, which relates the aperture field distribution to the far field distribution (see Chap. 15). For this reason, instruments based on this method are sometimes called digital lenses. The Fraunhofer equation is also the basis of the holographic method of measuring the surface accuracy of parabolic antennas, as described in Sect. 17.3.

---

[3]The SKA Memo Series can be found at http://www.skatelescope.org/publications.

Daishido et al. (1984) described the operation and prototype of a direct Fourier transform telescope operating at 11 GHz. They called the instrument a "phased array telescope" because its operation was equivalent to forming phased array beams pointed at a grid of positions on the sky. The Fourier transform was affected though the use of Butler matrices. A 64-element array (8×8 elements on a uniform grid) was built at Waseda University and used for wide-field searches of transient sources (Nakajima et al. 1992, 1993; Otobe et al. 1994). The signal processing was further improved in another instrument aimed at pulsar observations (Daishido et al. 2000; Takeuchi et al. 2005).

Interest has been renewed in the direct Fourier transform telescope because of the advent of arrays with very large numbers of antennas. In this case, the direct Fourier transform configuration can take advantage of the computational speed of the fast Fourier transform, which scales as $n_a \log_2 n_a$, where n_a is the number of antennas. A detailed analysis of the direct Fourier transform telescope was developed by Tegmark and Zaldarriaga (2009, 2010). They were motived by the challenges of measuring the wide-field distribution of redshifted HI emission, the signature of the Epoch of Reionization (see Sect. 10.7.2), and called their instrument the Fast Fourier Transform Telescope. Zheng et al. (2014) built a prototype 8×8 array at 150 MHz to develop techniques for such measurements.

One characteristic of the direct Fourier transform telescope based on the FFT with a uniform-grid antenna layout is the high redundancy of short baselines. The situation is similar to that encountered in the design of the digital FFT spectrometers described in Sect. 8.8.5, wherein the number of equivalent baselines at large spacings is underrepresented. Methods of relaxing the requirement of uniform spacings have been explored by Tegmark and Zaldarriaga (2010) and Morales (2011).

A disadvantage of the direct Fourier transform telescope relates to calibration. Since no baseline-based measurements are made, the traditional techniques of self-calibration based on amplitude and phase closure cannot be directly applied. There are several approaches to the calibration problem. The most straightforward approach is to transform the images back to the visibility domain on the time scale of instrumental and atmospheric variability, and apply the techniques described in Chap. 11. Auxiliary measurements can also be made to supply calibration information. More sophisticated methods are under development (e.g., Foster et al. 2014; Beardsley et al. 2016).

Further Reading

Baars, J.W.M., *The Paraboloidal Reflector Antenna in Radio Astronomy and Communication*, Springer, New York (2007)

Balanis, C.A., *Antenna Theory Analysis and Design*, Wiley, New York, 1982 (1997)

Collin, R.E., *Antennas and Radiowave Propagation*, McGraw-Hill, New York (1985)

Imbriale, W.A., and Thorburn, M., Eds., *Proc. IEEE*, Special Issue on Radio Telescopes, **82**, 633–823 (1994)

Johnson, R.C., and Jasik, H., Eds., *Antenna Engineering Handbook*, McGraw-Hill, New York (1984)

Kraus, J.D., *Antennas*, McGraw-Hill, New York, 1950, and 2nd ed., McGraw-Hill, New York, 1988. The 3rd ed. is Kraus, J.D., and Marhefka, R.J., *Antennas for All Applications*, McGraw-Hill, New York (2002)

Love, AW, Ed., *Reflector Antennas*, IEEE Press, Institute of Electrical and Electronics Engineers, New York (1978)

Milligan, T.A., *Modern Antenna Design*, McGraw-Hill, New York (1985)

Stutzman, W.L., and Thiele, G.A., *Antenna Theory and Design*, 2nd ed., Wiley, New York (1998)

References

Arsac, J., Nouveau réseau pour l'observation radioastronomique de la brillance sur le soleil à 9530 Mc/s, *Compt. Rend. Acad. Sci.*, **240**, 942–945 (1955)

Baars, J.W.M., *The Paraboloidal Reflector Antenna in Radio Astronomy and Communication*, Springer, New York (2007)

Baars, J.W.M., D'Addario, L.R., Thompson, A.R., Eds., *Proc. IEEE*, Special Issue on Advances in Radio Telescopes, **97**, 1369–1548 (2009)

Baars, J.W.M., and Hooghoudt, B.G., The Synthesis Radio Telescope at Westerbork: General Layout and Mechanical Aspects, *Astron. Astrophys.*, **31**, 323–331 (1974)

Beardsley, A.P., Thyagarajan, N., Bowman, J.D., and Morales, M.F., An Efficient Feedback Calibration Algorithm for Direct Imaging Radio Telescopes, *Mon. Not. R. Astron. Soc.*, in press (2016), arXiv:1603.02126

Blythe, J.H., A New Type of Pencil Beam Aerial for Radio Astronomy, *Mon. Not. R. Astron. Soc.* **117**, 644–651 (1957)

Bourke, T.L., Braun, R., Fender, R., Govoni, F., Green, J., Hoare, M., Jarvis, M., Johnston-Hollitt, M., Keane, E., Koopmans, L., and 14 coauthors, *Advancing Astrophysics with the Square Kilometre Array*, 2 vols., Dolman Scott Ltd., Thatcham, UK (2015) (available at http://www.skatelescope.org/books)

Bracewell, R.N., Interferometry of Discrete Sources, *Proc. IRE*, **46**, 97–105 (1958)

Bracewell, R.N., Interferometry and the Spectral Sensitivity Island Diagram, *IRE Trans. Antennas Propag.*, **AP-9**, 59–67 (1961)

Bracewell, R.N., Radio Astronomy Techniques, in *Handbuch der Physik*, Vol. 54, S. Flugge, Ed., Springer-Verlag, Berlin (1962), pp. 42–129

Bracewell, R.N., Optimum Spacings for Radio Telescopes with Unfilled Apertures, in *Progress in Scientific Radio*, Report on the 15th General Assembly of URSI, Publication 1468 of the National Academy of Sciences, Washington, DC (1966), pp. 243–244

Bracewell, R.N., *Two-Dimensional Imaging*, Prentice-Hall, Englewood Cliffs, NJ (1995)

Bracewell, R.N., *The Fourier Transform and Its Applications*, McGraw-Hill, New York (2000) (earlier eds. 1965, 1978).

Bracewell, R.N., Colvin, R.S., D'Addario, L.R., Grebenkemper, C.J., Price, K.M., and Thompson, A.R., The Stanford Five-Element Radio Telescope, *Proc. IEEE*, **61**, 1249–1257 (1973)

Bracewell, R.N., and Roberts, J.A., Aerial Smoothing in Radio Astronomy, *Aust. J. Phys.*, **7**, 615–640 (1954)

Bracewell, R.N., and Thompson, A.R., The Main Beam and Ringlobes of an East–West Rotation-Synthesis Array, *Astrophys. J.*, **182**, 77–94 (1973).

Braude, S. Ya., Megn, A.V., Ryabov, B.P., Sharykin, N.K., and Zhouck, I.N., Decametric Survey of Discrete Sources in the Northern Sky, *Astrophys. Space Sci.*, **54**, 3–36 (1978)

Brigham, E.O., *The Fast Fourier Transform and Its Applications*, Prentice Hall, Englewood Cliffs, NJ (1988)

Burke, B.F., Orbiting VLBI: A Survey, in *VLBI and Compact Radio Sources*, Fanti, R., Kellermann, K., and Setti, G., Eds., Reidel, Dordrecht, the Netherlands (1984)

Cane, H.V., Spectra of the Nonthermal Radio Radiation from the Galactic Polar Regions, *Mon. Not. R. Astron. Soc.*, **149**, 465–478 (1979)

Carilli, C., and Rawlings, S., Eds., Science with the Square Kilometre Array, *New Astron. Rev.*, **48**, 979–1605 (2004)

Chow, Y.L., On Designing a Supersynthesis Antenna Array, *IEEE Trans. Antennas Propag.*, **AP-20**, 30–35 (1972)

Chu, T.-S., and Turrin, R.H., Depolarization Effects of Offset Reflector Antennas, *IEEE Trans. Antennas Propag.*, **AP-21**, 339–345 (1973)

Cornwell, T.J., A Novel Principle for Optimization of the Instantaneous Fourier Plane Coverage of Correlation Arrays, *IEEE Trans. Antennas Propag.*, **36**, 1165–1167 (1988)

Daishido, T., Ohkawa, T., Yokoyama, T., Asuma, K., Kikuchi, H., Nagane, K., Hirabayashi, H., and Komatsu, S., Phased Array Telescope with Large Field of View to Detect Transient Radio Sources, in *Indirect Imaging: Measurement and Processing for Indirect Imaging*, Roberts, J.A., Ed., Cambridge Univ. Press, Cambridge, UK (1984), pp. 81–87

Daishido, T., Tanaka, N., Takeuchi, H., Akamine, Y., Fujii, F., Kuniyoshi, M., Suemitsu, T., Gotoh, K., Mizuki, S., Mizuno, K., Suziki, T., and Asuma, K., Pulsar Huge Array with Nyquist Rate Digital Lens and Prism, in *Radio Telescopes*, Butcher, H.R., Ed., Proc. SPIE, **4015**, 73–85 (2000)

DeBoer, D.R., Gough, R.G., Bunton, J.D., Cornwell, T.J., Beresford, R.J., Johnston, S., Feain, I.J., Schinckel, A.E., Jackson, C.A., Kesteven, M.J., and nine coauthors, Australian SKA Pathfinder: A High-Dynamic Range Wide-Field of View Survey Telescope, *Proc. IEEE*, **97**, 1507–1521 (2009)

de Vos, M., Gunst, A.W., and Nijboer, R., The LOFAR Telescope: System Architecture and Signal Processing, *Proc. IEEE*, **97**, 1431–1437 (2009)

Dewdney, P.E., Hall, P.J., Schilizzi, R.T., and Lazio, T.J.L.W., The Square Kilometre Array, *Proc. IEEE*, **97**, 1482–1496 (2009)

Dulk, G.A., Erickson, W.C., Manning, R., and Bougeret, J.-L., Calibration of Low-Frequency Radio Telescopes Using Galactic Background Radiation, *Astron. Astrophys.*, **365**, 294–300 (2001)

Ellingson, S.W., Antennas for the Next Generation of Low-Frequency Radio Telescopes, *IEEE Trans. Antennas Propag.*, **53**, 2480–2489 (2005)

Elmer, M., Jeffs, B.J., Warnick, K.F., Fisher, J.R., and Norrod, R.D., Beamformer Design Methods for Radio Astronomical Phased Array Feeds, *IEEE Trans. Antennas Propag.*, **60**, 903–914 (2012)

Erickson, W.C., Mahoney, M.J., and Erb, K., The Clark Lake Teepee-Tee Telescope, *Astrophys. J. Suppl.*, **50**, 403–420 (1982)

Foster, G., Hickish, J., Magro, A., Price, D., and Zarb Adami, K., Implementation of a Direct-Imaging and FX Correlator for the BEST-2 Array, *Mon. Not. R. Astron. Soc.*, **439**, 3180–3188 (2014)

Frater, R.H., Brooks, J.W., and Whiteoak, J.B., The Australia Telescope—Overview, in *J. Electric. Electron. Eng. Australia*, Special Issue on the Australia Telescope, **12**, 103–112 (1992)

Golomb, S.W., How to Number a Graph, in *Graph Theory and Computing*, Read, R.C., Ed., Academic Press, New York (1972), pp. 23–27

Hall, P.J., Ed., The Square Kilometre Array: An Engineering Perspective, *Experimental Astron.*, **17(1–3)** (2004) (also as a single volume, Springer, Dordrecht, the Netherlands, 2005)

Hamaker, J.P., O'Sullivan, J.D., and Noordam, J.E., Image Sharpness, Fourier Optics, and Redundant Spacing Interferometry, *J. Opt. Soc. Am.*, **67**, 1122–1123 (1977)

Hay, S.G., O'Sullivan, J.D., Kot, J.S., Granet, C., Grancea, A., Forsythe, A.R., and Hayman, D.H., Focal Plane Array Development for ASKAP, in *Antennas and Propagation*, Proc. European Conf. on Ant. and Prop. (2007)

Hirabayashi, H., Hirosawa, H., Kobayashi, H., Murata, Y., Edwards, P.G., Fomalont, E.B., Fujisawa, K., Ichikawa, T., Kii, T., Lovell, J.E.J., and 43 coauthors, Overview and Initial Results of the Very Long Baseline Interferometry Space Observatory Program, *Science*, **281**, 1825–1829 (1998)

Hjellming, R.M., The Design of Aperture Synthesis Arrays, *Synthesis Imaging in Radio Astronomy*, Perley, R.A., Schwab, F.R., and Bridle, A.H., Eds., Astron. Soc. Pacific. Conf. Ser., **6**, 477–500 (1989)

Ho, P.T.P., Moran, J.M., and Lo, K.-Y., The Submillimeter Array, *Astrophys. J. Lett.*, **616**, L1–L6 (2004)

Högbom, J.A., and Brouw, W.N., The Synthesis Radio Telescope at Westerbork, Principles of Operation, Performance, and Data Reduction, *Astron. Astrophys.*, **33**, 289–301 (1974)

Hotan, A.W., Bunton, J.D., Harvey-Smith, L., Humphreys, B., Jeffs, B.D., Shimwell, T., Tuthill, J., Voronkov, M., Allen, G., Amy, S., and 91 coauthors, The Australian Square Kilometre Array Pathfinder: System Architecture and Specifications of the Boolardy Engineering Test Array, *Publ. Astron. Soc. Aust.*, **31**, e041 (15pp) (2014)

Ingalls, R.P., Antebi, J., Ball, J.A., Barvainis, R., Cannon, J.F., Carter, J.C., Charpentier, P.J., Corey, B.E., Crowley, J.W., Dudevoir, K.A., and six coauthors, Upgrading of the Haystack Radio Telescope for Operation at 115 GHz, *Proc. IEEE*, **82**, 742–755 (1994)

Ishiguro, M., Minimum Redundancy Linear Arrays for a Large Number of Antennas, *Radio Sci.*, **15**, 1163–1170 (1980)

Ivashina, M.V., Iupikov, O., Maaskant, R., van Cappellen, W.A., and Oosterloo, T., An Optimal Beamforming Strategy for Wide-Field Survey with Phased-Array-Fed Reflector Antennas, *IEEE Trans. Antennas Propag.*, **59**, 1864–1875 (2011)

Jonas, J.L., MeerKAT—The South African Array with Composite Dishes and Wide-Band Single Pixel Feeds, *Proc. IEEE*, **97**, 1522–1530 (2009)

Kardashev, N.S., Khartov, V.V., Abramov, V.V., Avdeev, V.Yu., Alakoz, A.V., Aleksandrov, Yu.A., Ananthakrishnan, S., Andreyanov, V.V., Andrianov, A.S., Antonov, N.M., and 120 coauthors, "RadioAstron": A Telescope with a Size of 300,000 km: Main Parameters and First Observational Results, *Astron. Reports*, **57**, 153–194 (2013)

Keto, E., The Shapes of Cross-Correlation Interferometers, *Astrophys. J.*, **475**, 843–852 (1997).

Kogan, L., Level of Negative Sidelobes in an Array Beam, *Publ. Astron. Soc. Pacific*, **111**, 510–511 (1999)

Koles, W.A., Frehlich, R.G., and Kojima, M., Design of a 74-MHz Antenna for Radio Astronomy, *Proc. IEEE*, **82**, 697–704 (1994)

Lal, D.V., Lobanov, A.P., and Jiménez-Monferrer, S., Array Configuration Studies for the Square Kilometre Array: Implementation of Figures of Merit Based on Spatial Dynamic Range, Square Kilometre Array Memo 107 (2009)

Lawrence, C.R., Herbig, T., and Readhead, A.C.S., Reduction of Ground Spillover in the Owens Valley 5.5-m Telescope, *Proc. IEEE*, **82**, 763–767 (1994)

Leech, J., On Representation of 1, 2, ... , *n* by Differences, *J. London Math. Soc.*, **31**, 160–169 (1956)

Lobanov, A.P., Imaging with the SKA: Comparison to Other Future Major Instruments, Square Kilometre Array Memo 38 (2003)

Lonsdale, C.J., Cappallo, R.J., Morales, M.F., Briggs, F.H., Benkevitch, L., Bowman, J.D., Bunton, J.D., Burns, S., Corey, B.E., deSouza, L., and 38 coauthors, The Murchison Widefield Array: Design Overview, *Proc. IEEE*, **97**, 1497–1506 (2009)

Mangum, J.G., Baars, J.W.M., Greve, A., Lucas, R., Snel, R.C., Wallace, P., and Holdaway, M., Evaluation of the ALMA Prototype Antennas, *Publ. Astron. Soc. Pacific*, **118**, 1257–1301 (2006)

Mathur, N.C., A Pseudodynamic Programming Technique for the Design of Correlator Supersynthesis Arrays, *Radio Sci.*, **4**, 235–244 (1969)

Mayer, C.E., Emerson, D.T., and Davis, J.H., Design and Implementation of an Error-Compensating Subreflector for the NRAO 12-m Radio Telescope, *Proc. IEEE*, **82**, 756–762 (1994)

Meinel, A.B., Multiple Mirror Telescopes of the Future, in *The MMT and the Future of Ground-Based Astronomy*, Weeks, T.C., Ed., SAO Special Report 385 (1979), pp. 9–22

Mills, B.Y., Cross-Type Radio Telescopes, *Proc. IRE Aust.*, **24**, 132–140 (1963)

Moffet, A.T., Minimum-Redundancy Linear Arrays, *IEEE Trans. Antennas Propag.*, **AP-16**, 172–175 (1968)

Morales, M.F., Enabling Next-Generation Dark Energy and Epoch of Reionization Radio Observatories with the MOFF Correlator, *Pub. Astron. Soc. Pacific*, **123**, 1265–1272 (2011)

Nakajima, J., Otobe, E., Nishibori, K., Watanabe, N., Asuma, K., and Daishido, T., First Fringe with the Waseda FFT Radio Telescope, *Pub. Astron. Soc. Japan*, **44**, L35–L38 (1992)

Nakajima, J., Otobe, E., Nishibori, K., Kobayashi, H., Tanaka, N., Saitoh, T., Watanabe, N., Aramaki, Y., Hoshikawa, T., Asuma, K., and Daishido, T., One-Dimensional Imaging with the Waseda FFT Radio Telescope, *Pub. Astron. Soc. Japan*, **45**, 477–485 (1993)

Napier, P.J., Bagri, D.S., Clark, B.G., Rogers, A.E.E., Romney, J.D., Thompson, A.R., and Walker, R.C., The Very Long Baseline Array, *Proc. IEEE*, **82**, 658–672 (1994)

Napier, P.J., Thompson, A.R., and Ekers, R.D., The Very Large Array: Design and Performance of a Modern Synthesis Radio Telescope, *Proc. IEEE*, **71**, 1295–1320 (1983)

National Radio Astronomy Observatory, *A Proposal for a Very Large Array Radio Telescope*, National Radio Astronomy Observatory, Green Bank, WV, Vol. 1 (1967); Vol. 3, Jan. 1969.

Otobe, E., Nakajima, J., Nishibori, K., Saito, T., Kobayashi, H., Tanaka, N., Watanabe, N., Aramaki, Y., Hoshikawa, T., Asuma, K., and Daishido, T., Two-Dimensional Direct Images with a Spatial FFT Interferometer, *Pub. Astron. Soc. Japan*, **46**, 503–510 (1994)

Padin, S., Cartwright, J.K., Mason, B.S., Pearson, T.J., Readhead, A.C.S., Shepherd, M.C., Sievers, J., Udomprasert, P.S., Holzapfel, W.L., Myers, S.T., and five coauthors, First Intrinsic Anisotropy Observations with the Cosmic Background Imager, *Astrophys. J. Lett.*, **549**, L1–L5 (2001)

Papoulis, A., *Signal Analysis*, McGraw-Hill, New York (1977), p. 74

Perley, R., Napier, P., Jackson, J., Butler, B., Carlson, B., Fort, D., Dewdney, P., Clark, B., Hayward, R., Durand, S., Revnell, M., and McKinnon, M., The Expanded Very Large Array, *Proc. IEEE*, **97**, 1448–1462 (2009)

Preston, R.A., Burke, B.F., Doxsey, R., Jordan, J.F., Morgan, S.H., Roberts, D.H., and Shapiro, I.I., The Future of VLBI Observations in Space, in *Very-Long-Baseline Interferometry Techniques*, Biraud, F., Ed., Cépaduès Éditions, Toulouse, France (1983), pp. 417–431

Rabiner, L.R., and Gold, B., *Theory and Application of Digital Signal Processing*, Prentice-Hall, Englewood Cliffs, NJ (1975), p. 50

Rademacher, H., and Toeplitz, O., *The Enjoyment of Mathematics*, Princeton Univ. Press, Princeton, NJ (1957)

Raimond, E., and Genee, R., Eds., *The Westerbork Observatory, Continuing Adventure in Radio Astronomy*, Kluwer, Dordrecht, the Netherlands (1996)

Roshi, D.A., and Fisher, J.R., A Model for Phased Array Feed, Electronics Div. Internal Report 330, National Radio Astronomy Observatory, Charlottesville, VA (2016)

Rudge, A.W., and Adatia, N.A., Offset-Parabolic-Reflector Antennas: A Review, *Proc. IEEE*, **66**, 1592–1618 (1978)

Ruze, J., Antenna Tolerance Theory—A Review, *Proc. IEEE*, **54**, 633–640 (1966)

Ryle, M., The New Cambridge Radio Telescope, *Nature*, **194**, 517–518 (1962)

Ryle, M., and Hewish, A., The Synthesis of Large Radio Telescopes, *Mon. Not. R. Astron. Soc.*, **120**, 220–230 (1960)

Ryle, M., Hewish, A., and Shakeshaft, J.R., The Synthesis of Large Radio Telescopes by the Use of Radio Interferometers, *IRE Trans. Antennas Propag.*, **7**, S120–S124 (1959)

Schaubert, D.H., and Chio, T.H., Wideband Vivaldi Arrays for Large Aperture Arrays, in *Perspectives on Radio Astronomy: Technologies for Large Arrays*, Smolders, A.B., and van Haarlem, M.P., Eds., ASTRON, Dwingeloo, the Netherlands, pp. 49–57 (1999)

Seielstad, G.A., Swenson, G.W., Jr., and Webber, J.C., A New Method of Array Evaluation Applied to Very Long Baseline Interferometry, *Radio Sci.*, **14**, 509–517 (1979)

Snel, R.C., Mangum, J.G., and Baars, J.W.M., Study of the Dynamics of Large Reflector Antennas with Accelerometers, *IEEE Antennas Propag. Mag.*, **49**, 84–101 (2007)

Stewart, K.P., Hicks, B.C., Ray, P.S., Crane, P.C., Kassim, N.E., Bradley, R.F., and Erickson, W.C., LOFAR Antenna Development and Initial Observations of Solar Bursts, *Planetary Space Sci.*, **52**, 1351–1355 (2004)

Swarup, G., Ananthakrishnan, S., Kapahi, V.K., Rao, A.P., Subrahmanya, C.R., and Kulkarni, V.K., The Giant Metrewave Radio Telescope, *Current Sci.* (Current Science Association and Indian Academy of Sciences), **60**, 95–105 (1991)

Swenson, G.W., Jr. and Kellermann, K.I., An Intercontinental Array—A Next-Generation Radio Telescope, *Science*, **188**, 1263–1268 (1975)

Swenson, G.W., Jr., and Mathur, N.C., The Circular Array in the Correlator Mode, *Proc. IREE Aust.*, **28**, 370–374 (1967)

Takeuchi, H., Kuniyoshi, M., Daishido, T., Asuma, K., Matsumura, N., Takefuji, K., Niinuma, K., Ichikawa, H., Okubo, R., Sawano, A., and four coauthors, Asymmetric Sub-Reflectors for Spherical Antennas and Interferometric Observations with an FPGA-Based Correlator, *Pub. Astron. Soc. Japan*, **57**, 815–820 (2005)

Tegmark, M., and Zaldarriaga, M., The Fast Fourier Transform Telescope, *Phys. Rev. D*, **79**, 08530 (2009)

Tegmark, M., and Zaldarriaga, M., Omniscopes: Large Area Telescope Arrays with Only $N \log N$ Computational Cost, *Phys. Rev. D*, **82**, 103501(10 pp) (2010)

Thomasson, P., MERLIN, *Quart. J. R. Astron. Soc.*, **27**, 413–431 (1986)

Thompson, A.R., and Bracewell, R.N., Interpolation and Fourier Transformation of Fringe Visibilities, *Astron. J.*, **79**, 11–24 (1974)

Thompson, A.R., Clark, B.G., Wade, C.M., and Napier, P.J., The Very Large Array, *Astrophys. J. Suppl.*, **44**, 151–167 (1980)

Unser, M., Sampling—50 Years After Shannon, *Proc. IEEE*, **88**, 569–587 (2000)

van Ardenne, A, Bregman, J.D., van Cappellen, W.A., Kant, G.W., and Bij de Vaate, J.G., Extending the Field of View with Phased Array Techniques: Results of European SKA Research, *Proc. IEEE*, **97**, 1531–1542 (2009)

van Cappellen, W.A., and Bakker, L., APERTIF: Phased Array Feeds for the Westerbork Synthesis Radio Telescope, in Proc. IEEE International Symposium on Phased Array Systems and Technology (ARRAY), Boston, MA, Oct. 12–15 (2010), pp. 640–647

van Cappellen, W.A., Bakker, L., and Oosterloo, T.A., Experimental Results of the APERTIF Phased Array Feed, in Proc. 30th URSI General Assembly and Scientific Symposium, Istanbul, Turkey, Aug. 13–20 (2011), 4 pp

van Haarlem, M.P., Wise, M.W., Gunst, A.W., Heald, G., McKean, J.P., Hessels, J.W.T., de Bruyn, A.G., Nijboer, R., Swinbank, J., Fallows, R., and 191 coauthors, LOFAR: The LOw-Frequency ARray, *Astron. Astrophys.*, **556**, A2 (53pp) (2013)

Walker, R.C., VLBI Array Design, in *Indirect Imaging*, J. A. Roberts, Ed., Cambridge Univ. Press, Cambridge, UK (1984), pp. 53–65

Welch, J., Backer, D., Blitz, L., Bock, D., Bower, G.C., Cheng, C., Croft, S., Dexter, M., Engargiola, G., Fields, E., and 36 coauthors, The Allen Telescope Array: The First Widefield, Panchromatic, Snapshot Radio Camera for Radio Astronomy and SETI, *Proc. IEEE*, **97**, 1438–1447 (2009)

Welch, W.J., Thornton, D.D., Plambeck, R.L., Wright, M.C.H., Lugten, J., Urry, L., Fleming, M., Hoffman, W., Hudson, J., Lum, W.T., and 27 coauthors, The Berkeley–Illinois–Maryland Association Millimeter Array, *Publ. Astron. Soc. Pacific*, **108**, 93–103 (1996)

Wild, J.P., A New Method of Image Formation with Annular Apertures and an Application in Radio Astronomy, *Proc. R. Soc. Lond. A*, **286**, 499–509 (1965)

Wild, J.P., Ed., *Proc. IREE Aust.*, Special Issue on the Culgoora Radioheliograph, **28**, No. 9 (1967)

Williams, W.F., High Efficiency Antenna Reflector, *Microwave J.*, **8**, 79–82 (1965) [reprinted in Love (1978); see Further Reading]

Wootten, A., and Thompson, A.R., The Atacama Large Millimeter/Submillimeter Array, *Proc. IEEE*, **97**, 1463–1471 (2009)

Zheng, H., Tegmark, M., Buza, V., Dillon, J., Gharibyan, H., Hickish, J., Kunz, E., Liu, A., Losh, J., Lutomirski, A., and 28 coauthors, Mapping Our Universe in 3D with MITEoR, in Proc. IEEE International Symposium on Phased Array Systems and Technology, Waltham, MA (2013), pp. 784–791

Zheng, H., Tegmark, M., Buza, V., Dillon, J.S., Gharibyan, H., Hickish, J., Kunz, E., Liu, A., Losh, J., Lutomirski, A., and 27 coauthors, MITEoR: A Scalable Interferometer for Precision 21 cm Cosmology, *Mon. Not. R. Astron. Soc.*, **445**, 1084–1103 (2014)